J Seismol
https://doi.org/10.1007/s10950-024-10229-0

RESEARCH

Comparison between rupture parameters of intermediate and deep earthquakes at the Peru–Brazil–Bolivia border and northern Chile

Carmen Pro · Hernando Tavera · Maurizio Mattesini · Lucía Escudero · Elisa Buforn · Agustín Udías · Estela Centeno

Received: 7 March 2024 / Accepted: 24 June 2024

Abstract We determined the main parameters of the source rupture process of intermediate- and deep-depth earthquakes occurring in the Peru–Brazil–Bolivia border region and northern Chile. The parameters of depth, fault-plane orientation, scalar seismic moment, slip distribution, and radiated seismic energy are obtained from seismograms. We selected 15 intermediate-depth earthquakes ($100\ km < h < 300\ km$) and 10 very deep earthquakes ($h > 500\ km$) with magnitudes $M_W \geq 6.0$. For most events, the slip distribution over the rupture plane shows a single asperity, and the source time function presents a simple pulse. There are differences between intermediate-depth and deep earthquakes. The rupture areas, maximum slip and source time function (STF) duration are larger for intermediate-depth events than for deep events. Additionally, the STF's show a sharper increase for deep earthquakes. The scaled radiated seismic energy shows larger values for deep depth events. The stress regime pattern derived from the obtained focal mechanism agrees with the geometry of the subduction of the Nazca plate. At intermediate depths, in the northern area up to 12°S, the stress pattern corresponds to a horizontal extension, while in the southern area, the tension axes dip at an angle of 30°. At deep depths, the stress regime corresponds to vertical compression in the north and dips of approximately 45° in the south.

Keywords Intermediate- and deep-depth earthquakes · Kinematic inversion · Source rupture parameter differences · Nazca plate subduction

Highlights
1. Rupture source parameters of intermediate and deep-depth earthquakes in Peru-Bolivia-Brazil-northern Chile.
2. Differences on rupture area, maximum slip, STF and scaled energy between intermediate-depth and deep earthquakes.
3. The differences can provide information about the rupture process with depth in subduction regions.

Supplementary Information The online version contains supplementary material available at https://doi.org/10.1007/s10950-024-10229-0.

C. Pro (✉)
Dpto de Física- Centro Universitario de Mérida, Universidad de Extremadura, 06800 Mérida, Spain
e-mail: cpro@unex.es

H. Tavera · E. Centeno
Instituto Geofísico del Perú, Lima, Perú

M. Mattesini · L. Escudero · E. Buforn · A. Udías
Dpto. de Física de La Tierra y Astrofísica, Universidad Complutense, 28040 Madrid, Spain

1 Introduction

The goal of the present study is to analyze the source and rupture parameters of intermediate-depth ($100\ km < h < 300\ km$) and deep-depth ($h > 500\ km$) earthquakes, specifically focusing on focal depth, fault-plane orientation, scalar seismic moment,

Published online: 09 July 2024

radiated energy, source time function, slip distribution, effective rupture area, rupture velocity, and stress drop. The study area encompasses the region of Peru–Brazil–Bolivia border region and northern Chile (henceforth PBBNC), which is defined by latitudes 1°S to 20°S and longitudes 65°W to 80°W. Since both types of earthquakes are located in the same region, we will be able to better analyze the dependence of the parameters on depth. Campus and Das (2000) affirm that different tectonic regions exhibit different behaviors in some cases. In various subduction zones, there are large-scale differences in seafloor age, which affect slab temperature and deep earthquake properties (Zhan 2020).

The use of a homogeneous database in this work is crucial for making a rigorous comparison between the rupture parameters of intermediate-depth and deep earthquakes. For this reason, we estimated the rupture parameters for the selected earthquakes directly from seismograms using the same methodology for both intermediate-depth and deep events, avoiding the use of source parameters determined by other authors or methodologies. In this way, the comparison between the obtained parameters could reveal more precisely if the rupture processes for the intermediate-depth and deep events are different. The strength of this work resides in the fact that we have estimated the rupture parameters for the selected earthquakes—both of intermediate-depth and deep- directly from the seismograms using the same methodology. Our analysis is based on parameters such as depth, fault plane orientation, source time function, slip, scalar seismic moment and radiated seismic energy, all obtained directly from observations. Other parameters derived from them may be affected by uncertainties, such as the static stress drop or the seismic efficiency, so we are not considering those. The values of the source parameters for these earthquakes will help us to understand the nature of the processes taking place at intermediate-depth and deep-depth earthquakes and the relationships between their source parameters in this particular area.

Recent studies have analyzed variations in source parameters with depth for a group of selected intermediate-depth earthquakes located in different subduction zones. For instance, in Japan, Ko and Kuo (2016) found an increase of stress drop with depth and observed low values of radiation efficiency for events deeper than 60 km. Similarly, Nishitsuji and Mori (2014) also obtained values of radiation efficiency slightly lower than those for shallow earthquakes. However, for Northern Chile, Derode and Campos (2019) found that rupture velocities, stress drop, and radiation efficiency are higher for intermediate-depth than for shallow earthquakes. On the other hand, Megawati et al. (2024) obtained for intermediate-depth earthquakes located in Java stress drop values similar to those of shallow earthquakes. For deep-depth earthquakes, we have also found studies that examine the relationship between rupture parameters and depth. For example, Tibi et al. (2003) observed different behaviours for large deep earthquakes from different subduction zones, depending on the temperature of the subducting plate. They obtained low rupture velocity values for events in warm slabs. Park and Mori (2008) also obtained low rupture velocity values for large deep earthquakes around Japan. Suzuki and Yagi (2011), applying the back projection method to large deep-depth earthquakes in various subductions zones, obtained low values for rupture velocity except within the depth range of 530 to 610 km.

Some researchers have studied the rupture parameters of both intermediate and deep-depth earthquakes, seeking evidence of differences in rupture that could be related to variations in the physical models of earthquake generation. Several works were focused on comparing the duration and shape of the source time function (Houston et al. 1998; Persh and Houston 2004; Tocheport et al.2007) and have found that the scaled duration is shorter for deep than for intermediate-depth earthquakes. It was also observed that the STFs show more complexity for events occurring at depths between 350 and 550 km. Poli and Prieto (2016) found that the stress drop is invariant with depth, while apparent stress and radiation efficiency increase with depth. Rodkin (2022), analyzing data from the world GCMT seismic moment catalog, found that the apparent stress and the averaged normalized rupture duration versus depth representation exhibit maxima values at different depth intervals (less than 15 km, 40–50 km, 120–150 km and 500–600 km) corresponding to the depth intervals of different earthquake generation models. As we have mentioned before, these studies examined variations in source parameters with depth for earthquakes located in different areas and did not specifically focus on the PBBNC region. Given the diversity of deep event properties, it is important to isolate the variations linked to the rupture process.

The seismicity in the region of PBBNC is a consequence of the subduction of the Nazca plate beneath the South American plate. This subduction process occurs at an average velocity of 7–8 cm/year in an approximately west−east direction, generating many earthquakes at intermediate and deep depths of moderate to large magnitudes. This is due to large deformation across the convergent boundary zone, with the Peruvian Andes representing the most significant surface expression of this deformation (Norabuena et al 1998; Villegas-Lanza et al 2016; Tamay et al 2021).

Figures 1a and b show the seismicity for the studied region (period of 1960–2021, M > 4.5; Instituto Geofísico del Perú). The shallow earthquakes (h ≤ 60 km, red circles in Figs. 1a and b) are distributed in two zones parallel to the coast, mainly between the trench and the coast; there is an area where epicenters are concentrated in the southern zone between 14°S and 20°S. In the interior of the continent, shallow earthquakes are less frequent, and they are mainly concentrated along the Sub-Andean zone (SAZ) and Eastern Cordillera (EC) (Fig. 1a), with moderate magnitudes (generally less than 6.0). Intermediate-depth earthquakes (60 km < h ≤ 300 km, green circles in Fig. 1a and b) are distributed in a different pattern from north to south. Between latitudes 2°S and 10°S, most of them occur inside the continent, and a few foci occur offshore, with a concentration of seismic foci at approximately latitudes 8°S-10°S and at longitude 74°W (SAZ) near the Brazilian border (Wagner and Okal 2019). From latitudes 14°S to 20°S, the number of

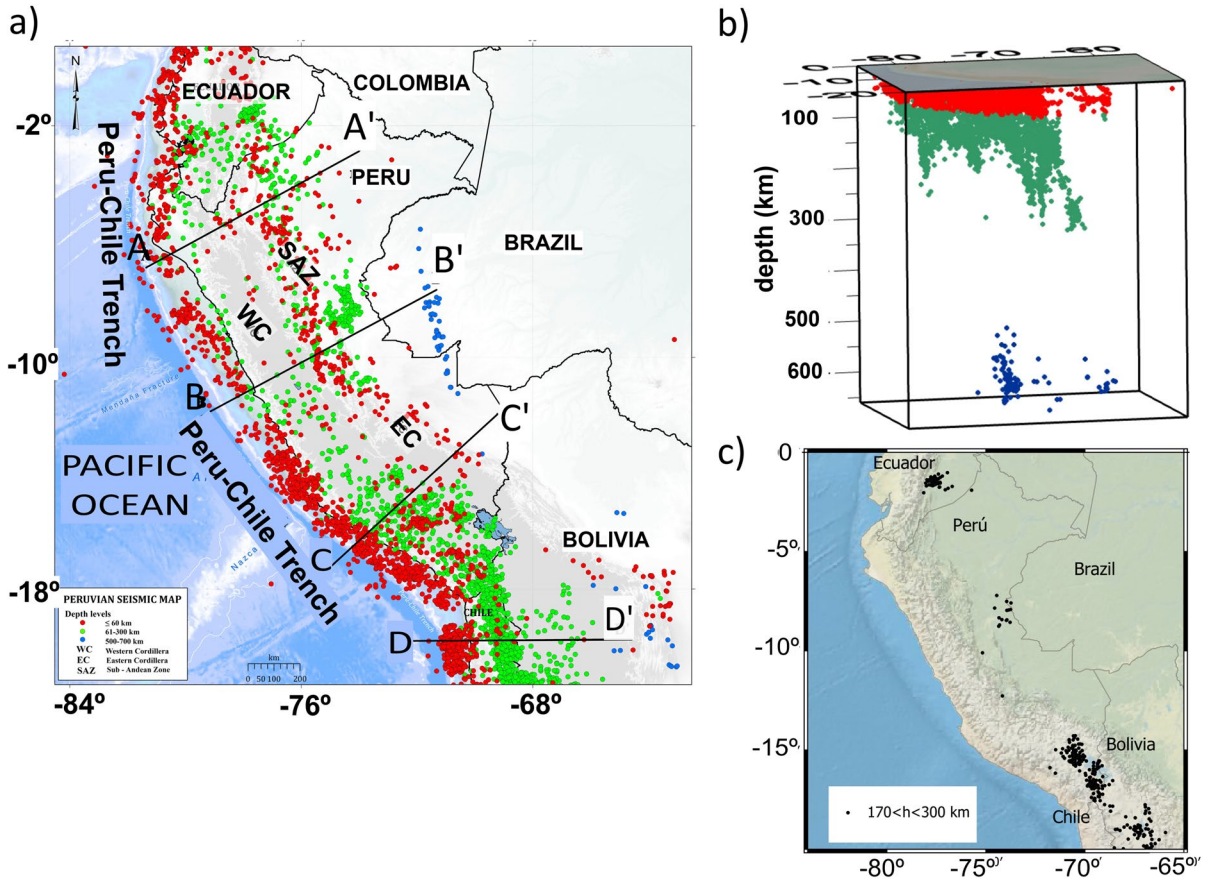

Fig. 1 Seismicity for the studied region (1960–2021, M > 4.5): (**a**) distribution of epicenters and (**b**) hypocenters (Instituto Geofísico del Perú). Red circles correspond to shallow events (h < 100 km), green circles correspond to intermediate events (100 km < h < 300 km) and blue circles correspond to deep events (h > 500 km). SAZ: Sub-Andean zone; EC: Eastern Cordillera; WC: Western Cordillera. Lines AA', BB', CC' and DD' correspond to the vertical cross-sections shown in Fig. 2; (**c**) distribution of epicenters for earthquakes with 170 km < h < 300 km

intermediate-depth earthquakes increases, and a large number of earthquakes occur in land parallel to the coast. Deep seismic activity (h > 500 km, blue circles in Fig. 1a and b) is distributed in two zones (Fig. 1a). The first zone, on the Peru–Brazil border contains great activity, with epicenters distributed over a wide area in an approximately NNW−SSE direction. In the second zone, in central Bolivia, the epicenters are also more concentrated. A general overview of the earthquake depth distribution is shown in Fig. 1b, where the depth gap between intermediate-depth and deep earthquakes is clearly visible. Additionally, we observe that the intermediate foci with 170 < h < 300 km are not uniformly distributed. In Fig. 1c we observe that they are mostly concentrated in three zones: Ecuador, central Peru close to the Peru-Brazil border and southern region of Peru and Bolivia- Chile border. This distribution agrees with Rodkin (2022), who proposes that earthquakes occur in a series of narrow layers whose depths are different in the various subduction zones.

To study the depth distribution of seismicity, four vertical cross-sections perpendicular to the trench from north to south are shown in Figs. 1 and 2. Cross-section AA' (Fig. 1a), which corresponds to the northern region of Peru (Fig. 2a), shows shallow offshore earthquakes (depths less than 60 km) between the trench and approximately 1000 km inside the continent, with a gap between 400 and 500 km. The intermediate-depth activity starts at a distance of 250 km from the section origin, following a 30° slope until reaching a depth of 120 km at a distance of 400 km, and then the earthquakes are distributed mostly horizontally until reaching distances of 700 km. The depths increase from 120 to 180 km between distances of 700 km and 800 km, where intermediate-depth activity stops. In this section, no deep-depth activity is observed. Cross-section BB' (Fig. 1a) corresponds to the central region of Peru, and here, the shallow-depth earthquakes show a major concentration (Fig. 2b) at distances between 100 and 300 km and between 500 and 700 km from the origin. The intermediate-depth earthquakes are distributed following a 30° slope up to distances of 900 km from the trench, with a horizontal distribution between 400 and 600 km, reaching a maximum depth of 200 km at the eastern end of the section. Deep earthquakes (depths of 500 km and 650 km) are located at distances between 850 and 1200 km and are detached from intermediate-depth earthquakes. For the southern Peru region, in cross-section CC' (Fig. 1a), the shallow-depth activity (Fig. 2c) is distributed from the trench to 800 km, with a decrease in the number of

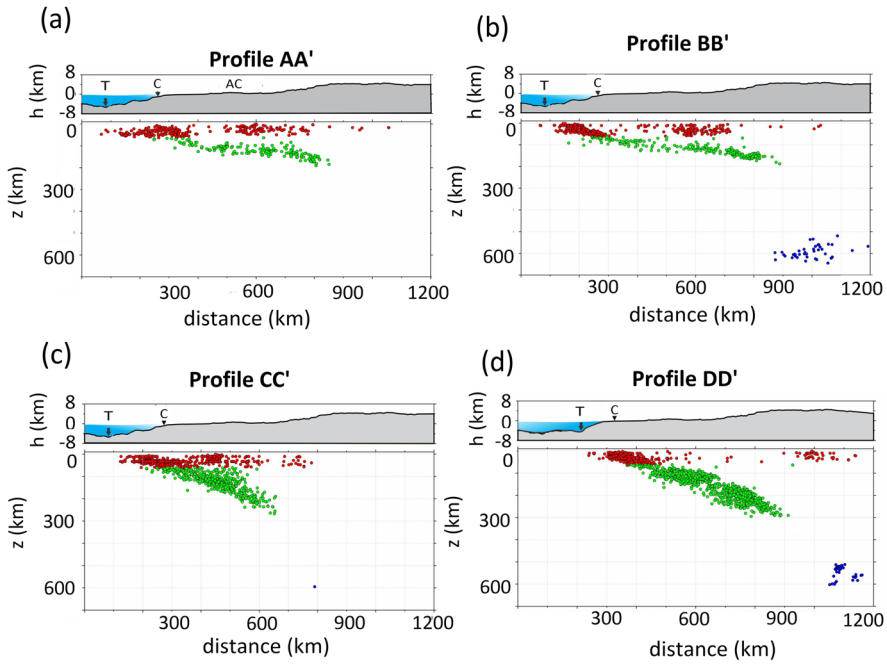

Fig. 2 Vertical cross-sections (**a**: AA', **b**: BB', **c**: CC', and **d**: DD') with 360 km bandwidth projection for the 1960–2021 period. Red circles correspond to shallow events (h < 100 km), green circles correspond to intermediate events (100 km < h < 300 km) and blue circles correspond to deep events (h > 500 km). T: trench, C: coast, AC: Andean Cordillera

earthquakes from a distance of 500 km. The distribution of intermediate-depth earthquake follows a line from 200 to 650 km with a slope of 30°, reaching a maximum depth of 300 km. This slope value is similar to the dipping slab observed by Phillips et al. (2012) in southern Peru, based on receiver function and tomographic studies. They developed a model extending from the coast to 300 km inside inland, showing that the margin crust is underthrust by the Brazilian Shield, which could extend beneath the entire Altiplano. There is only one deep earthquake (depth of 600 km) located at a distance of 800 km from the coast. Finally, cross-section DD' (Fig. 1a), located in northern Chile, shows shallow earthquakes (Fig. 2d) between distances of 200 km and 1200 km. The large concentration of earthquakes occurs at distances of approximately 300 km to 500 km, with a clear decrease to a distance of 900 km. Another group of shallow earthquakes, which are less numerous, is located between 900 and 1000 km. The intermediate-depth earthquakes follow a similar alignment (slope 30°) to that of cross-section CC' from distances of 400 km to 900 km, reaching a maximum depth of 300 km. The deep earthquakes are detached from the intermediate-depth earthquakes and are located between depths of 500 km and 600 km at distances from 1050 to 1150 km from the coast.

In the region under study, the distribution of earthquakes with depth, shown in the four cross-sections (Figs. 1 and 2), corresponds to the geometry of the subduction of the Nazca plate beneath the South American continent in the studied region. At intermediate depths, the subducting slab has a flat part, which is subhorizontal at a depth of 120 km, in the north–central regions (cross-sections AA' and BB') and dips approximately 30° in the southern region (cross-sections CC' and DD') due to an increase in the curvature of the Nazca plate. The deep earthquakes are located in two places: the Peru–Brazil border and central Bolivia (Fig. 1). There is a lack of earthquakes between depths of 300 and 500 km (cross-sections BB' and DD'), so the two groups of intermediate- and deep-depth earthquakes are clearly separated by a 200 km depth interval (Fig. 2) (Cahill and Isacks 1992; Lindo et al. 1992; Norabuena et al. 1994; Spence et al. 1999; Tavera and Buforn 2001; Hayes et al. 2012; Lim et al. 2018; Wagner and Okal 2019; Tavera 2023).

2 Data and methodology

For our study, we selected 25 earthquakes, 15 at intermediate depths ($100 < h < 300$ km) and 10 at very deep depths ($h > 500$ km), with magnitudes M_W between 5.9 and 8. These earthquakes occurred between 1997 and 2021 (Table 1, Fig. 3). The data were taken from BDSN (2014), SCSN (1926), Caribbean Network (2006), GEOSCOPE (1982), GEOFON (1993), GTSN (1993), GSN IRIS/IDA (1986), GSN IRIS/USGS (2014) and IMS (1965) networks. We assume these earthquakes to be representative of the intermediate- and deep-depth seismicity in the region. The selected earthquakes follow two approximately NNW−SSE alignments: one inside the continent and one parallel to the coast. The intermediate-depth earthquakes are closer to the coast and form two groups: a northern group with epicenters in northern Peru and Ecuador and a southern group with epicenters in southern Peru, western Bolivia and northern Chile. The deep earthquakes are farther from the coast and concentrated in the Peru–Brazil border area and farther south in Bolivia.

The data that were used are seismograms recorded at epicentral distances of 30°- 90° and were retrieved from the Incorporated Research Institutions for Seismology (IRIS Data Manager Center, http://ds.iris.edu/wilber3/find_event), deconvolved with the instrument response, converted to ground displacement, and then filtered using a Butterworth bandpass filter between 0.01 and 1 Hz to eliminate the low frequencies introduced after the integration process. The high frequencies present in some records are due to noise and have not been modeled. The Earth model that was used corresponds to the IASPEI91 model (Kennett and Engdahl 1991).

We first estimated the following source parameters: fault plane orientation, focal depth, scalar seismic moment, rupture velocity, maximum slip, rupture area, source time function (STF), and stress drop. These parameters have been obtained from the slip inversion over the fault plane of teleseismic body waves (Kikuchi and Kanamori 1991) with Green's functions generated using the IASPEI91 Earth model.

We used a two-step procedure. In the first step, a kinematic point source model was used to obtain the fault plane orientation and focal depth from the inversion of the body waves. Several inversions were carried out using different depth ranges. In the

Table 1 Intermediate and deep depth earthquakes used in this study (IRIS database)

event	date	time (UTC)	longitude (°)	latitude (°)	h (km)	Mw
1	2021–11-28	10:52:14	-76.811	-04.453	126	7.5
2	2019–05-26	07:41:15	-75.278	-05.813	122	8.0
3	2018–11-01	22:19:51	-69.266	-19.583	106	6.2
4	2018–01-21	01:06:42	-69.445	-18.881	117	6.3
5	2017–01-02	13:13:48	-76.368	-04.895	111	5.9
6	2016–09-10	10:08:20	-76.954	-05.573	122	6.1
7	2015–03-23	04:51:38	-69.166	-18.353	131	6.4
8	2012–11-10	14:57:50	-75.071	-08.866	124	6.0
9	2012–08-02	09:38:30	-74.259	-08.414	150	6.0
10	2012–06-07	16:03:18	-72.413	-15.877	108	6.1
11	2012–05-14	10:00:40	-69.591	-17.678	110	6.3
12	2011–08-24	17:46:11	-74.530	-07.640	150	7.0
13	2011–03-06	12:31:59	-69.360	-18.020	112	6.2
14	2010–08-12	11:54:15	-77.310	-01.270	208	7.1
15	2010–05-23	22:46:51	-74.432	-14.000	103	6.1
16	2018–08-24	09:04:08	-70.828	-11.035	625	7.0
17	2016–12-18	13:30:10	-70.970	-09.974	636	6.5
18	2015–11-26	05:45:18	-71.257	-09.182	611	6.7
19	2015–11-24	22:45:38	-70.944	-10.537	619	7.5
20	2011–11-22	18:48:16	-65.090	-15.360	568	6.6
21	2010–05-24	16:18:29	-71.560	-08.090	581	6.4
22	2007–07-21	13:27:04	-71.270	-08.130	637	6.0
23	2003–06-20	06:19:38	-71.720	-07.610	562	7.0
24	2002–10-12	20:09:11	-71.740	-08.300	534	6.9
25	1997–11-28	22:53:41	-68.790	-13.740	615	6.7

second step, we used an extended source at a fixed depth corresponding to the best result obtained in the first step. The rupture area is estimated from the inversion of the observed body waves. We divided the fault plane into a square grid using a grid with cell sizes that varied from 6×6 km to 20×20 km, depending on the earthquake magnitude. To estimate the rupture velocity, we carried out the inversion with different values within an interval that covered a wide range, from 2.5 km/s to 3.5 km/s for intermediate-depth earthquakes and from 2.5 km/s to 4.5 km/s for deep earthquakes, with increments of 0.5 km/s. For each rupture velocity value, we analyzed the slip distribution, the shape and duration of the STF and the adjustment between the observed and theoretical waveforms. The final rupture velocity value corresponds to the minimum variance value in this adjustment. This rupture velocity value is then used to determine the effective rupture area. In this determination, we considered only the subfaults with seismic moments greater than or equal to 0.1 times the maximum scalar seismic moment. Other authors took this factor to be between 0.1 to 0.2 (Lay et al. 2013; Ye et al. 2013, 2016a).

The slip distribution was estimated for each earthquake for the two planes. The average static stress drop was calculated using the relationship between the seismic moment (M_0) and fault area (S), $\Delta\sigma = \frac{7M_0}{16}\left(\frac{\pi}{S}\right)^{3/2}$ given by Kanamori and Anderson (1975).

We estimated the radiated seismic energy (E_R) from the velocity spectrum using the single-station method (Boatwrigth and Choy, 1986; Venkataraman and Kanamori, 2004; Poli and Prieto 2016). The spectra were computed for the direct P-waves used to obtain focal mechanisms (Supplementary Material). We removed the instrument response to obtain the velocity spectra from 0.01 to 1.5 Hz. Each spectrum

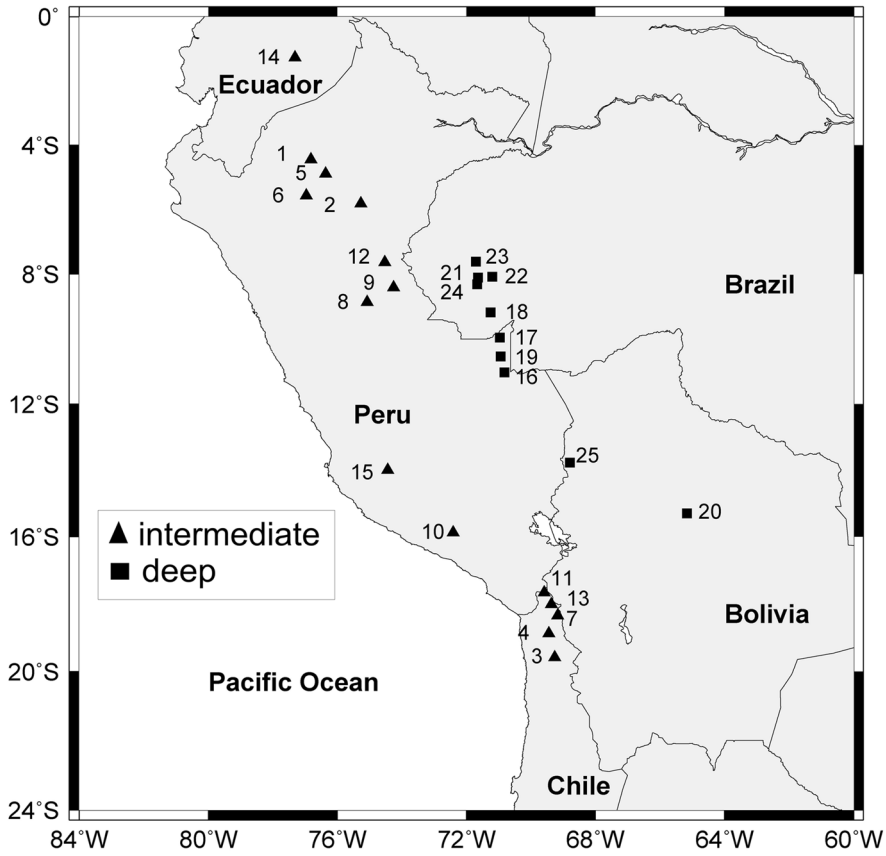

Fig. 3 Epicentral locations of the 15 intermediate-depth earthquakes (100 km < h < 300 km, triangles) and the 10 deep earthquakes (h > 500 km, squares) in this study (taken from IRIS)

was corrected for geometrical spreading, attenuation ($t^* = 0.3$, Poli and Prieto 2016), the free surface effect, and the radiation pattern of each station according to the estimated focal mechanism. Finally, we obtained the apparent stress using the relation $\sigma_a = \mu E_R / M_0$, considering the change of the shear modulus μ with the depth as a linear function. The results for intermediate-depth and deep earthquakes are given in Tables 2 and 3, respectively.

As an example of the procedure that was used, the best results of the inversion for intermediate-depth event 14 (Table 1 and Fig. 3) are shown in Fig. 4. At the top of the figure, the values of the obtained scalar seismic moment ($M_0 = 5.59 \times 10^{19}$ Nm), the moment magnitude ($M_W = 7.1$), the focal depth (h = 212 km) and the rupture velocity ($v_r = 2.5$ km/s) are presented. In the center, (a) the root mean square error (rms) between the observed and synthetic waveforms (for the point source model) versus depth shows the minimum at h = 212 km, and (b) the chosen fault plane solution, which corresponds to the minimum rms, is presented along with the observations used in the inversion. The fault plane solution corresponds to a nearly horizontal plane (156°, 16°, and -67°) and a nearly vertical plane (313°, 75°, and -97°). On the right (c), the source time function (STF) is shown with a duration of 11 s, which was obtained using the extended source model (the second step), with a fixed rupture velocity of 2.5 km/s and a depth of 212 km. Finally, at the bottom (d), we show the slip distribution over the rupture plane for the horizontal plane with an effective rupture area of 904 km^2 and a radius of 17 km for a circular fault, together with the value of the maximum slip of 2.16 m. A stress drop of 5.0 MPa and 1.8×10^{15} J of radiated seismic energy were obtained. The slip distribution for the vertical plane is provided in Supplementary Material.

3 Results for intermediate-depth earthquakes

Following the above-described procedure, we determined the source and rupture parameters of 15 intermediate-depth earthquakes (Table 2 and Fig. 5). In

Table 2 Focal parameters for intermediate depth earthquakes

Event	Date	M_0 ($\times 10^{19}$ Nm)	Mw	h (km)	strike/dip/slip (°)	v_r (km/s)	Δu_{max} (m)	S (km^2)	$\Delta\sigma$(MPa)	STF duration (s)	E_R (J)	σ_a(MPa)
1	2021–11-28	20.70	7.5	125	338.2/38.0/-89.2	3.0	1.48	5095	1.4	25	1.9×10^{15}	0.6
2	2019–05-26	123.00	8.0	145	342.8/62.5/-93.9	3.0	2.71	19,340	1.1	66	4.7×10^{16}	2.5
3	2018–11-01	0.39	6.3	108	167.0/ 14.6/ -93.9	3.0	0.52	340	1.5	6	7.8×10^{13}	1.2
4	2018–01-21	0.42	6.4	120	176.6/16.8/ -95.9	3.0	0.48	394	1.3	5	4.8×10^{13}	0.7
5	2017–01-02	0.13	6.0	112	359.0/41.4/-68.2	3.0	0.13	566	0.2	4	3.0×10^{12}	0.1
6	2016–09-10	0.31	6.3	125	9.8/ 32.7/-61.2	3.0	0.28	450	0.8	8	9.1×10^{12}	0.2
7	2015–03-23	0.74	6.5	132	247.1/18.8/-25.9	3.0	0.23	1106	0.5	11	1.7×10^{14}	1.5
8	2012–11-10	0.16	6.1	125	27.0/ 38.1/ -70.8	3.0	0.07	786	0.2	6	1.3×10^{13}	0.4
9	2012–08-02	0.20	6.1	150	196.6/19.5/-82.0	3.0	0.11	718	0.3	9	4.1×10^{12}	0.1
10	2012–06-07	0.28	6.2	110	107.5/33.1/176.9	3.0	0.10	1144	0.2	8	3.1×10^{13}	0.7
11	2012–05-14	0.40	6.3	108	202.0/ 20.9/ -8.7	3.0	0.44	393	1.3	5	2.9×10^{14}	4.4
12	2011–08-24	5.81	7.1	155	339.1/ 59.3/ -108.1	2.5	2.06	1157	3.6	10	1.4×10^{15}	1.6
13	2011–03-06	0.35	6.3	127	235.1/ 22.9/ -18.1	3.0	0.15	766	0.4	9	6.8×10^{13}	1.3
14	2010–08-12	5.59	7.1	212	156.5/ 16.5/ -67.1	2.5	2.16	904	5.0	11	1.8×10^{15}	2.4
15	2010–05-23	0.296	6.2	103	321.4/ 37.8/-94.2	3.0	0.10	1129	0.2	9	1.4×10^{13}	0.2

M_0 = Scalar seismic moment; M_w = moment magnitude, h = focal depth; v_r = rupture velocity; Δu_{max} = maximum slip; S = effective area; $\Delta\sigma$ = stress drop; STF = source time function; E_R = radiated seismic energy; σ_a = apparent stress

Table 3 Focal parameters for deep-depth earthquakes

Event	Date	M_0 ($\times 10^{19}$ Nm)	Mw	h (km)	strike/dip/slip (°)	v_r (km/s)	Δu_{max} (m)	S (km^2)	$\Delta\sigma$(MPa)	STF duration (s)	E_R (J)	σ_a(MPa)
16	2018–08-24	4.12	7.0	655	149.0/55.0/-94.0	3.0	1.07	802	4.4	13.0	1.0×10^{15}	3.0
17	2016–12-18	0.40	6.3	645	168.1/67.3/-117.0	3.5	0.08	803	0.4	8.0	8.0×10^{13}	2.4
18	2015–11-26	1.00	6.6	620	163.2/62.8/-98.9	2.5	0.14	1692	0.4	8.0	1.0×10^{14}	1.2
19	2015–11-24	15.40	7.4	625	158.6/52.3/-107.4	2.5	1.05	2837	2.5	17.5	3.0×10^{15}	2.3
20	2011–11-22	0.57	6.4	585	175.3/8.9/111.8	2.5	0.12	1091	0.4	6.0	3.8×10^{14}	7.6
21	2010–05-24	0.40	6.3	580	156.1/57.0/-112.5	3.0	0.08	1053	0.3	10	3.0×10^{13}	0.9
22	2007–07-21	0.14	6.0	655	164.8/66.8/-109.6	2.5	0.12	222	1.0	6.5	6.0×10^{13}	5.2
23	2003–06-20	4.51	7.0	580	138.9/45.5/-115.2	3.0	0.16	4683	0.3	18.0	2.8×10^{14}	0.7
24	2002–10-12	0.92	6.6	545	145.9/48.4/-116.7	3.0	0.19	863	1.1	20.0	4.0×10^{14}	4.7
25	1997–11-28	0.72	6.5	605	13.7/ 19.8/ -23.1	3.0	0.26	615	1.2	5.0	2.3×10^{14}	3.7

M_0 = Scalar seismic moment; M_w = moment magnitude, h = focal depth; v_r = rupture velocity; Δu_{max} = maximum slip; S = effective area; $\Delta\sigma$ = stress drop; STF = source time function; E_R = radiated seismic energy; σ_a = apparent stress

the Supplementary Material, the results obtained from the slip inversion are given for each event, along with the fit of the observed and synthetic seismograms (Fig. S1-S15). For each earthquake, two solutions are shown (a and b), giving the slip distribution for each of the two planes of the fault plane solution. In Fig. 5, a summary of these results is represented on a map showing the fault plane solution, the STF and the slip distribution over the rupture plane for each earthquake. To choose the rupture plane from the two possible planes obtained in the inversion (see Supplementary Material; the chosen planes correspond to solution a), we considered the slip distribution and preferred the solution that has fewer asperities. This choice is based on the observation that for these events the waveforms are generally very simple within the selected frequency range.

Geographically, earthquakes can be divided into two groups. In the northern area (0° to 12°S), events 1, 2, 5, 6, 8, 9, 12, and 14 take place, while in the southern area (12°S to 20°S), events 3, 4, 7, 10, 11, 13 and 15 occur. Moment magnitudes vary from 6.0 to 6.5 (Table 2), except for the four larger events, namely, events 2 ($M_W = 8.0$), 1 ($M_W = 7.5$), 12 ($M_W = 7.1$) and 14 ($M_W = 7.1$), which are all located in the northern group. The focal depths obtained for all the earthquakes (Table 2) are similar to those given by IRIS (Table 1), with differences of less than 6 km. The only exceptions are for event 2 (145 km in our solution versus 122 km in IRIS) and for event 13 (127 km in our solution versus 112 km in IRIS).

The earthquakes in the northern area have very similar focal mechanism solutions (Fig. 5, Table 2), corresponding to normal faulting, with planes oriented nearly N−S and dipping approximately 45° and T axes horizontal in nearly an E−W orientation (P axes are nearly vertical). The only exception is event 14, the most northern event, which has dip-slip motion on an almost vertical plane in the NNW−SSE direction, T and P axes dipping 45°, T oriented NE and P oriented SW. The rupture areas are between 450 km^2 and 786 km^2, and the maximum slip varies from 0.07 to 2.67 m, depending on the magnitude of the earthquakes. The rupture velocity used is 3 km/s, except for events 12 and 14, which have 2.5 km/s. The STFs duration ranges from 4 to 10 s, except for the four largest magnitude events, which have longer durations: 2 (66 s), 1 (25 s), 12 (11 s) and 14 (11 s). These

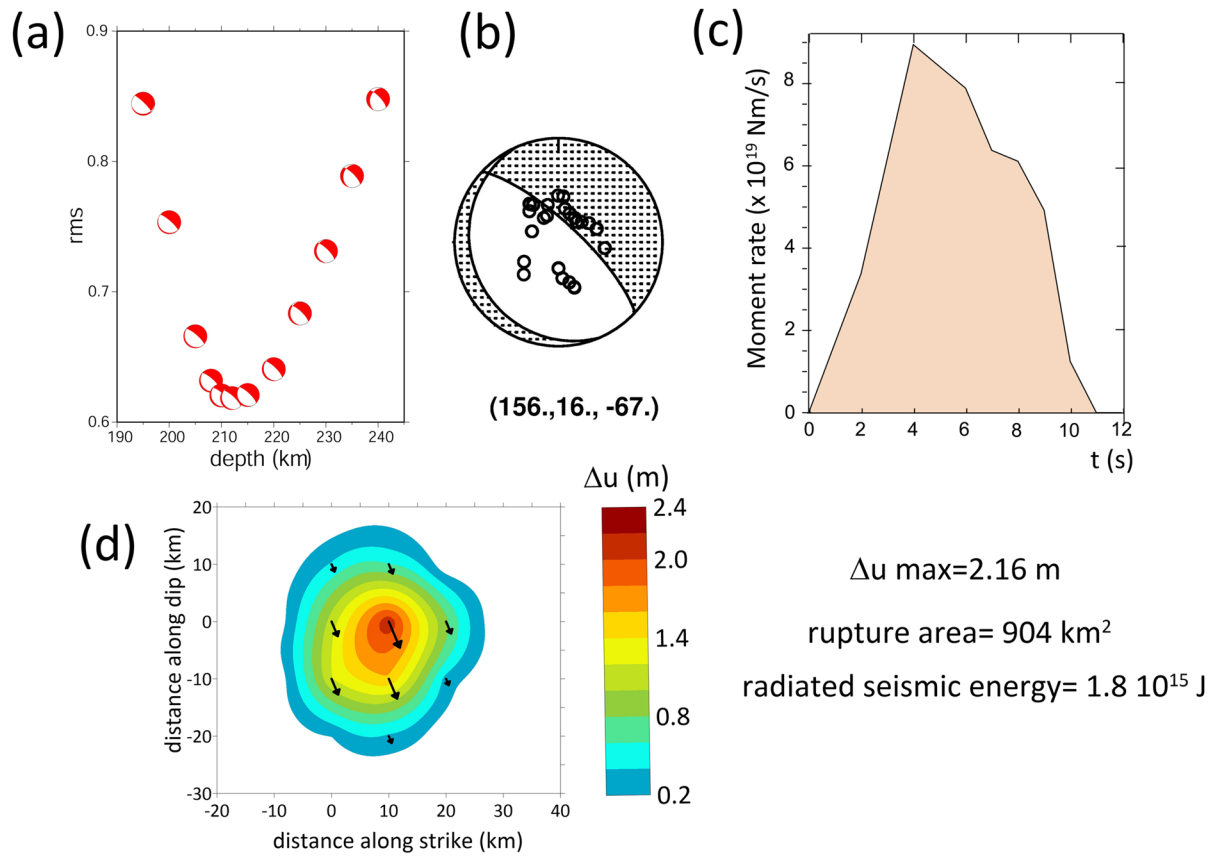

Fig. 4 Source parameters obtained for intermediate-depth event 14 (Table 1 and 2): (**a**) rms between the observed and synthetic waveforms (point source model) versus depth; (**b**) fault plane solution; (**c**) source time function (extended source); and (**d**) rupture area and slip distribution over the rupture plane

four earthquakes also have the largest rupture areas and radiated energy: 2 (19,340 km^2, 4.7×10^{16} J), 1 (5095 km^2, 1.9×10^{15} J), 12 (1157 km^2, 1.4×10^{15} J) and 14 (904 km^2, 1.8×10^{15} J). The shapes of the STFs are similar and simple, except for event 2.

As shown in Fig. 5 and Table 2, the earthquakes in the southern area have similar focal mechanisms, with a vertical plane in the N−S direction and the other plane that is nearly horizontal, except for event 15, with the planes dipping approximately 45°. Events 3, 4, 7, and 13 have T axes dipping 28°-35° to the east, while for events 10 and 11, the mechanism is similar but with the vertical plane oriented NW−SE for event 10 and NE−SW for event 11. Event 15 has dip-slip faulting, with planes oriented NNW−SSE and dipping 45°. The largest effective rupture areas correspond to events 10, 5 and 7 (1144 km^2, 1129 km^2 and 1106 km^2, respectively). Event 13 has an area of 766 km^2, and events 3, 4 and 11 have similar areas, i.e., 340 km^2, 394 km^2 and 393 km^2, respectively. In relation to the radiated energy, the largest values correspond to events 7 and 11, with 1.7×10^{14} J and 2.9×10^{14} J, respectively. For events 11, 13, 7, 4 and 3, located in northern Chile, Cabrera et al. (2021) obtained a slip distribution similar to that obtained in our study but with considerably smaller dimensions and using rupture velocities lower than 2.5 km/s. The STFs are simple with a short duration (less than 10 s), except for event 13, which has a complex duration, and events 7 and 15, which have longer durations (11 s).

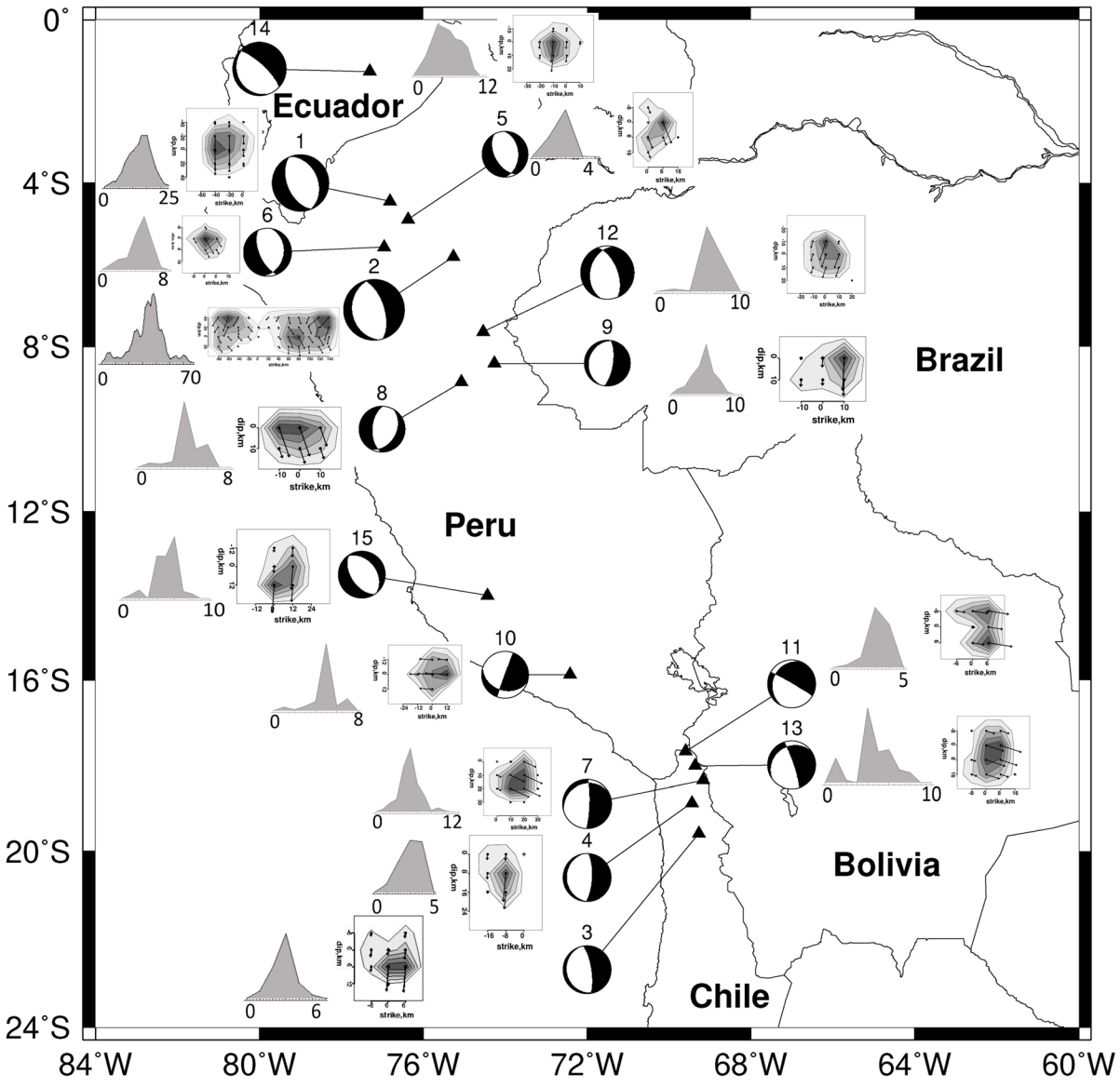

Fig. 5 Fault plane solutions, STFs, and slip distribution obtained for the 15 selected intermediate-depth earthquakes

A particular case, given the complexity of the slip distribution and the largest STF among the studied earthquakes, is event 2 ($M_W = 8$) at a depth of 145 km (Fig. 6 and Fig. S2a and b). The complex slip distribution for the vertically marked plane corresponds to an asymmetric bilateral rupture with three asperities, two of which are close in the northern part and the other in the southern part, with a maximum slip of 2.7 m and a rupture velocity of 3 km/s. The rupture starts close to the hypocenter and propagates along the rupture plane to the SSE. The second subevent occurs 10 s later, starting a bilateral rupture that also propagates to the NNE and extends along the width of the rupture plane with a larger release of energy. The third subevent (interval of 30–50 s) occurs 30 s after the beginning of the rupture, with the largest amount of energy released in a bilateral propagation extending along the width of the rupture plane. Finally, at 50 s, the propagation to the south stops, and only a small amount of energy propagating to the NNE is observed. This process is

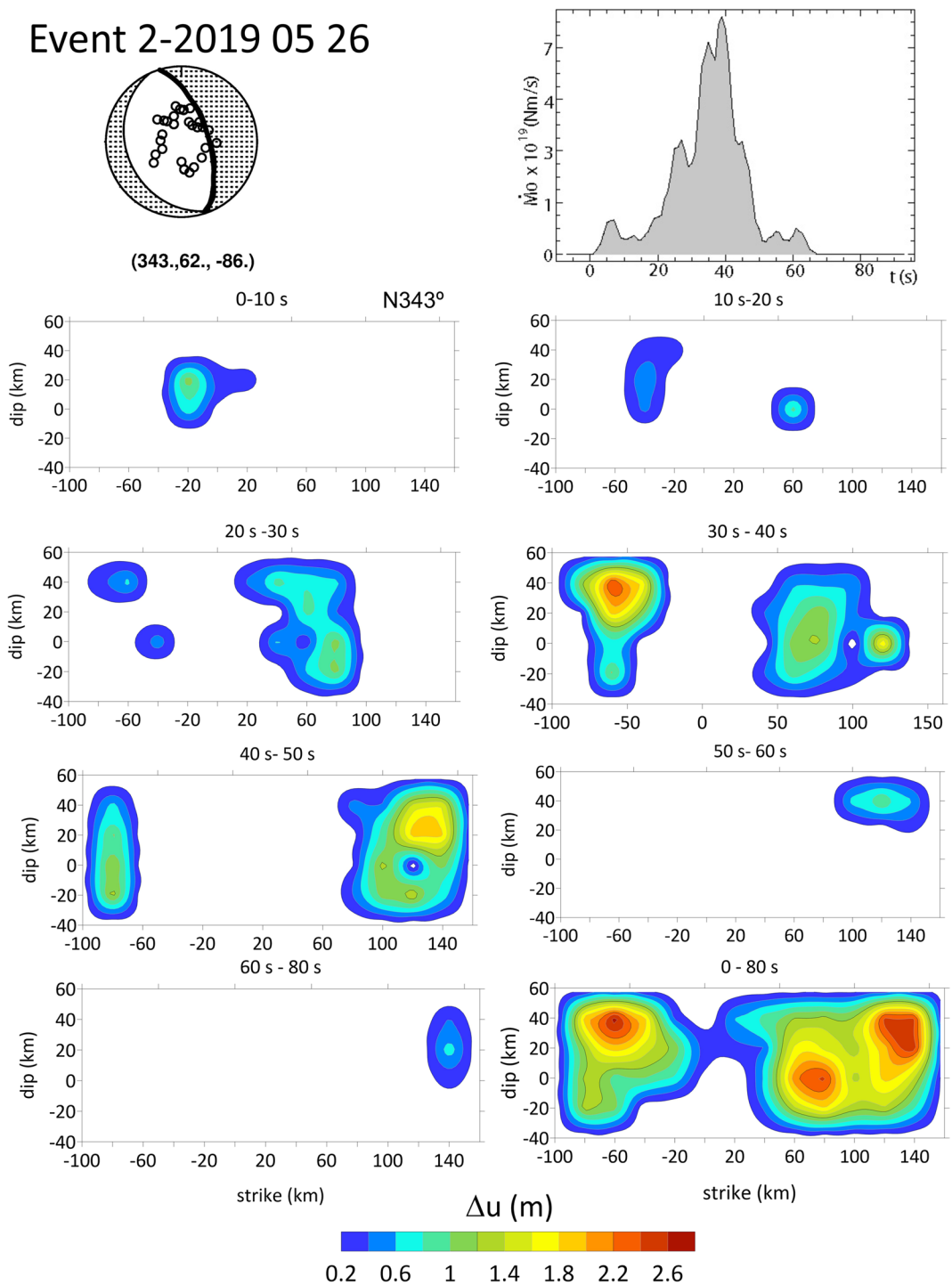

Fig. 6 Temporal history of the rupture for intermediate-depth event 2: Top left is the fault-plane solution (circles correspond to stations used in the inversion) and on the right is the moment rate function. The total slip distribution is shown in the bottom right

shown by the complex STF, with a duration of 70 s, corresponding to the different episodes of energy release, with three main pulses. For the horizontal plane, the distribution is similar (Fig. S2b). This result is similar to those obtained for this earthquake by other authors. Ye et al. (2020) reported a complex slip distribution with three patches, the rupture propagating northward at 3 km/s, and an STF duration of 66 s. Hu et al. (2021), indicated a rupture with a higher rupture velocity (4 km/s) in several episodes, beginning down-dip and eastward, following northward and then a bilateral rupture episode propagating both northward and southward and concluding with a unilateral northward rupture episode Liu and Yao (2020)proposed a rupture that is mainly unilaterally N−NW, with three high-slip areas, a lower STF duration (55 s), an average rupture velocity of 2.7 km/s and a maximum slip of 2 m.

4 Results for deep earthquakes

Of the selected 10 deep earthquakes (numbers 16 to 25) eight (16, 17, 18, 19, 21, 22, 23, and 24) are located at the Peru–Brazil border (PBB) and two (20 and 25) are located in Bolivia (Fig. 7), and their depths range from 545 to 655 km. The criteria used to choose the rupture plane are the same as those used for intermediate-depth earthquakes (Supplementary Material, solution a). Our depths (Table 3) are similar to those given by IRIS (differences of less than 10 km, Table 1), except for events 16 and 22 (with differences between 18 and 30 km). The moment magnitudes for the largest three are 19 ($M_W = 7.4$), 16 ($M_W = 7.0$) and 23 ($M_W = 7.4$), and the rest range between 6.3 and 6.6. A summary of the rupture parameters (fault plane solution, source time functions and slip distributions over the fault area) for these events is shown in Fig. 7 and Table 3 (the details of the results for each event are shown in Supplementary Material).

The nine events located at the PBB have the same focal mechanisms as those of normal dip-slip motion with planes oriented in the nearly N–S direction, dipping approximately 45° (Fig. 7) and with a nearly horizontal T axis in the E−W direction and a vertical P axis. Two earthquakes (25 and 20) (Fig. 7) are located in Bolivia to the south of the PBB group. Their focal mechanisms are different, showing dip-slip motion with a nearly vertical plane oriented in the NW−SE direction; the other plane is nearly horizontal, and the P and T axes dip approximately 45° in the NE−SW direction.

The effective rupture areas vary from 222 km^2 (event 22, M_W 6.0) to 4683 km^2 (event 23, M_W 7) (Fig. 7, Table 3). The slip distributions have a single asperity, except for events 24 and 16, which have two asperities. The maximum slips vary from 0.08 m (events 18 and 21, M_W 6.6 and 6.3) to 1.07 m (event 16, M_W 7). For earthquakes 17, 18, 20, 21, 22, and 25, the STFs correspond to single ruptures with very simple and narrow short durations, ranging from 2 to 10 s. Events 16, 19, and 23 have wider pulses of approximately 15 s to 20 s. The radiated seismic energy ranges from 3.0×10^{13} J to 3.0×10^{15} J for event 21 and event 19, respectively.

Event 24 ($M_W = 6.6$) at a depth of 545 km is a special case for deep earthquakes because it presents a complex rupture formed by three subevents with similar time durations (Fig. 8). For the plane dipping 48° in the NNW direction, the first subevent (duration of 3 s) starts at a depth of 545 km, with the rupture propagating downward. The rupture stops, and the second subevent (with a 3 s duration) starts 6 s later and propagates downward, but now in the SSE direction. The rupture stops again, and 3 s later starts again, with a larger duration (5 s) propagating downward toward the SSE. Most of the energy is released in the second subevent. The process is shown by the complex STF with three pulses and a total duration of 30 s (Fig. 8). This result agrees with those obtained by previous researchers (Houston et al. 1998; Persh and Houston 2004; Tocheport et al. 2007), who found that earthquakes between depths of 350 km and 550 km have more complex STFs. For the other plane, the slip distribution is similar (Fig. S15- S25).

Let´s now consider the 24 November 2015 earthquake doublet, which consists of two deep events that occurring 316 s and 55 km apart. In this work, we have studied the first one (event 19) obtaining a depth equal to 625 km, a magnitude $M_W = 7.4$ and a normal faulting mechanism with nodal planes in NS direction. We preferred the nodal plane dipping toward the west (strike 158.6º), with a propagating rupture velocity of 2.5 km/s, rupture duration 17.5 s and stress drop 2.5 MPa. The calculated radiated energy is equal to 3.0×10^{15} J. Ye et al. (2016b) also preferred this nodal plane because of the directivity effect observed at stations in the southern Pacific. They obtained a similar stress drop value (2.3 MPa)

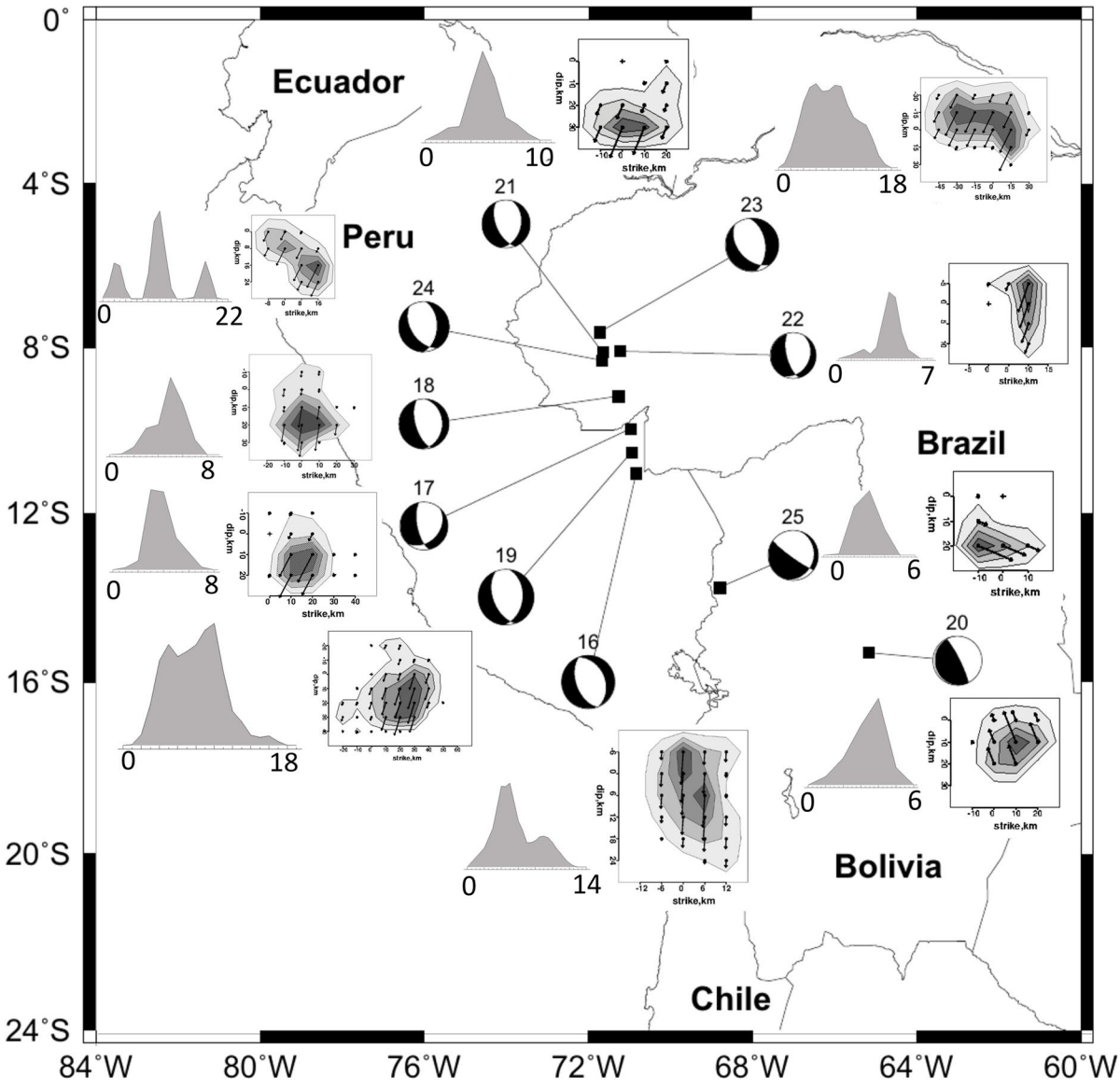

Fig. 7 Fault plane solutions, STFs, and slip distributions obtained for the 10 selected deep earthquakes

and radiated energy (4.2×10^{15} J), but a higher rupture propagation speed (4.5 km/s). Zahradník et al. (2017) also preferred the same plane from the tectonic context and rupture speeds of 2–3 km/s. Ruiz et al. (2017) also choose the plane dipping westward and obtained similar rupture velocity (2.25 km/s) and radiated energy (3.2×10^{15} J), but a higher stress drop (8.4 MPa). Jiménez et al. (2021) showed similar results to our work but a higher focal depth (655 km) and STF duration (20 s).

5 Relation between source parameters and focal depth

The nature and origin of intermediate-depth and deep-depth earthquakes in subduction zones are subject to different explanations. Some authors propose that the same mechanism, such as plastic instability instead of brittle failure, could explain the origin of both types (Roberts and Turcotte 2000), while others propose that deep earthquakes could differ from

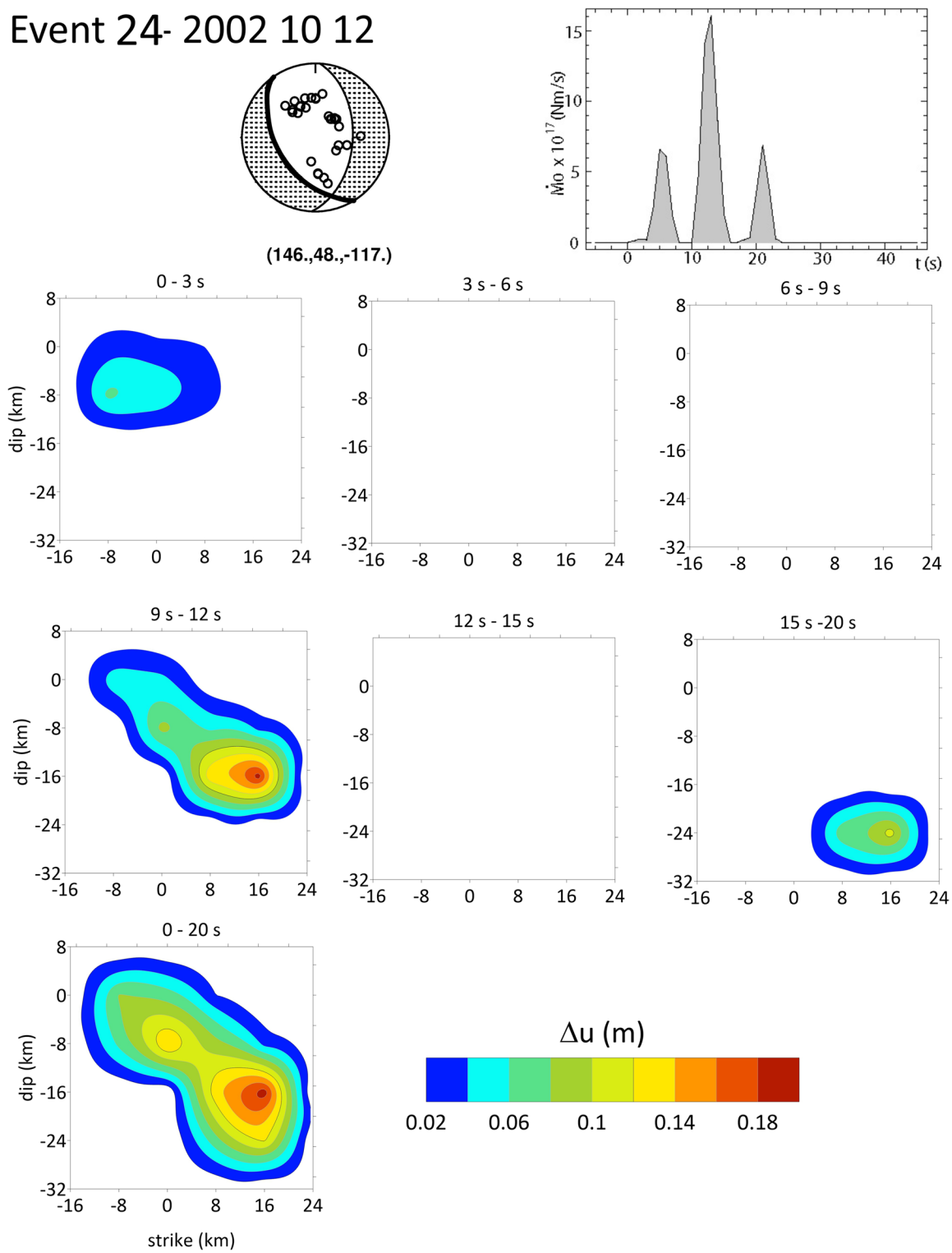

Fig. 8 Temporal history of the rupture for the deep event 24: Top left is the fault-plane solution (circles correspond to stations used in the inversion) and on the right is the moment rate function. The total slip distribution is shown in the bottom right

intermediate-depth earthquakes because of the rising pressure and temperature with depth. In this case, for intermediate-depth earthquakes, models have been proposed based on dehydration embrittlement of the subducting slab (Hacker et al. 2003; Okazaki and Hirth 2016) or viscous shear heating instabilities (John et al. 2009; Prieto et al. 2013), while for deep earthquakes, explanations have been proposed in terms of transformational faulting triggered by metastable olivine transforming to spinel (Green 2007), thermal instability (Kanamori et al.1998; Karato et al. 2001) or dehydration embrittlement (Omori et al. 2004). On the other hand, Rodkin (2022) proposed that the dominant factor of generation of the intermediate-depth earthquakes (with depths since 30–50 until 100–120 km) is high-pressure fluid, while the origin of the of the deeper earthquakes is related with solid-state phase transformations.

Previous works analyzed the values of the source parameters for intermediate-depth and deep-depth earthquakes, seeking differences in their generation processes. The STF's duration, stress drop, and radiated energy are usually compared. For instance, Tocheport et al. (2007) determined the source time function (STF) and moment tensor of intermediate-depth and deep earthquakes of worldwide and found that the scaled STF duration decreases with depth (about 9 s at intermediate depths while it is about 6 s for very deep earthquakes). Furthermore, they showed that the deepest events present systematically the simplest shapes, with greater complexity observed in the depth range 350 to 550 km. However, in relation to the radiated energy (E_R) and seismic moment (M_0) no variation with depth was observed in the E_R/M_0 versus M_0 relationship. In contrast, Vallée (2013) analyzing the SCARDEC STF database, found that deeper earthquakes have a larger stress drop, which is attributed to the rigidity increase in the Earth. This implies that the strain drop remains constant, suggesting that a simple mechanism could be responsible for all earthquakes. On the other hand, Poli and Prieto (2016) estimated stress drop, apparent stress, and radiation efficiency from rupture duration and radiated energy for deep and intermediate-depth earthquakes in various subduction zones. They concluded that stress drop is mostly independent of depth but, apparent stress increases with depth. Additionally, there is an average increment of radiation efficiency with depth.

The source parameters we determined for intermediate-depth and deep earthquakes can provide relevant information regarding their differences and the relationship between them. First, fault plane solutions are all very similar. For intermediate-depth earthquakes, there are two types of mechanisms: dip-slip normal faulting with planes in the approximately N−S direction and dipping approximately 45° degrees and dip-slip vertical faulting in the approximately N−S direction, mainly in the southern part. Both have mostly horizontal T axes in the east−west direction and vertical P axes. For deep earthquakes, except earthquakes 25 and 20, which have dip-slip vertical faulting, all earthquakes also have a mechanism of normal faulting similar to that of intermediate-depth earthquakes. Their relationship with the tectonic setting of the subduction zone in the region will be explained later.

Figure 9 shows the relationship between the obtained parameters a) effective rupture area (S), b) maximum slip (Δu max), c) duration of source time function (STF), and d) radiated energy (E_R) with scalar seismic moment (M_0). As expected, in all cases, the values of the parameters increase with the earthquakes size given by M_0. Also, Fig. 9 shows no difference between the relationship of the parameter values between intermediate-depth (triangles) and deep (squares) earthquakes.

The effective rupture areas of the intermediate-depth earthquakes range between 340 km^2 and 19,340 km^2, corresponding to magnitudes between 6 and 8, while those of deep-depth earthquakes range between 222 km^2 and 4683 km^2, corresponding to magnitudes between 6.0 and 7.4 (Tables 2 and 3). In Fig. 9a, we show the effective rupture area versus the scalar seismic moment with the corresponding stress drop values. We observe that the stress drop values are approximately the same for intermediate-depth and deep earthquakes, which is in agreement with the results shown by Poli and Prieto (2016). Most values are in the range of 0.3 to 1.5 MPa, and the highest values correspond to two intermediate-depth events, 14 (5.0 MPa) and 12 (3.6 MPa), and deep event 16 (4.4 MPa) (Tables 2 and 3). These earthquakes are the deepest among the intermediate-depth events in each case (h = 155 and 212 km) and some of the deepest among the deep events (655 km).

To compensate for the effect of the size, we divided the rupture areas by the seismic moment and represented

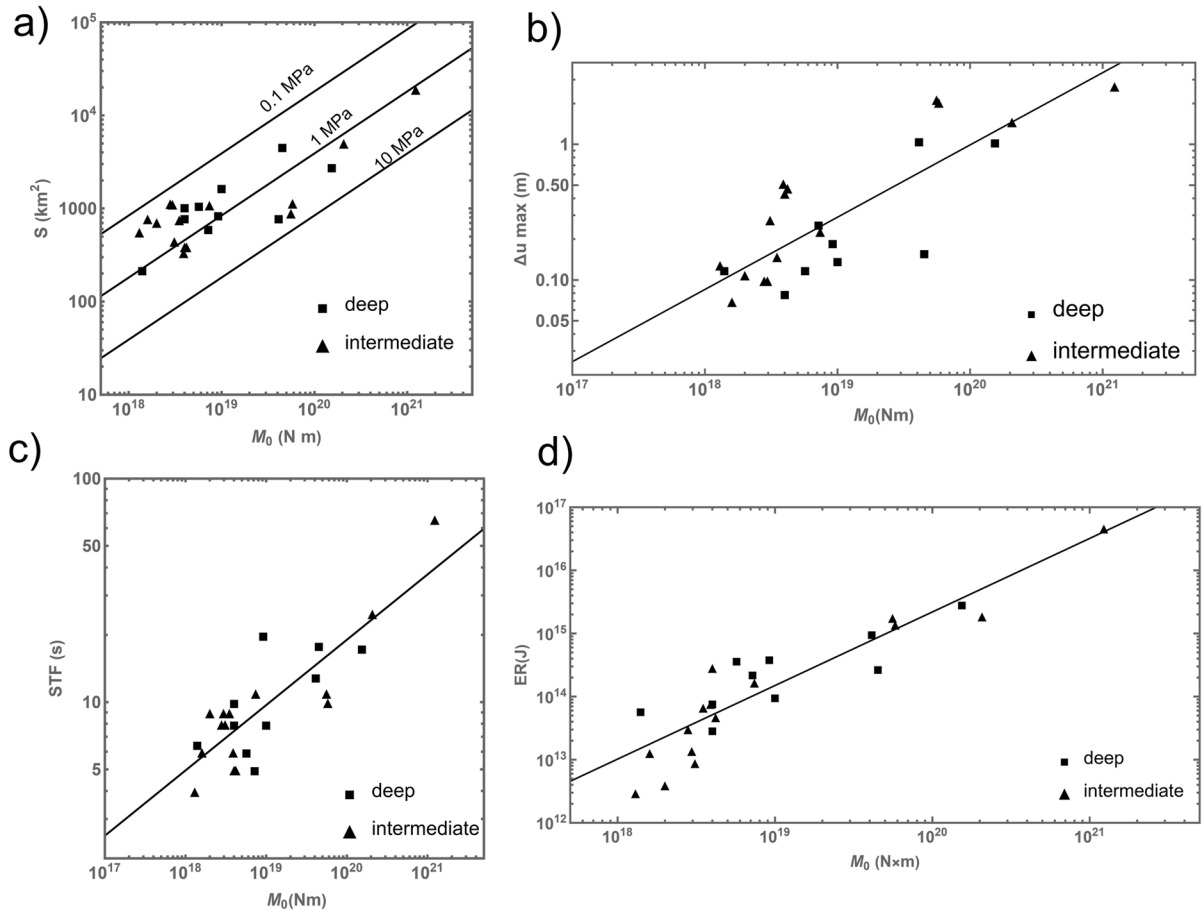

Fig. 9 Rupture parameters versus scalar seismic moment for intermediate-depth and deep earthquakes: (a) Effective rupture area with corresponding stress drop values, (**b**) maximum slip, (**c**) STF duration and (**d**) radiated energy E_R. The black lines correspond to the resulting fits

the resulting values versus depth (Fig. 10). The values for intermediate-depth earthquakes are slightly higher than those for deep-depth earthquakes, as shown by the mean values (Fig. 10, dotted line) for the two groups: $(2.0\pm0.4)\times10^{-10}$ m/N and $(1.3\pm0.3)\times10^{-10}$ m/N for intermediate-depth and deep-depth earthquakes, respectively. For intermediate-depth earthquakes, the lowest values (approximately 2×10^{-11} m/N) correspond to events with magnitude $M_W \geq 7.1$, located in the northern region (latitudes from 0° to 10°S), where there is flat subduction. For deep-depth earthquakes, the lowest values correspond to events with magnitude $M_W \geq 7.0$ located in the Peru- Brazil border. Therefore, we can conclude that for intermediate-depth and deep-depth earthquakes of similar size, the rupture areas are approximately the same, with some higher values for intermediate-depth earthquakes.

The values of maximum slip (Δu_{max}) for intermediate-depth earthquakes vary from 0.07 m to 2.71 m, corresponding to magnitudes between 6 and 8, and for deep-depth earthquakes, they vary between 0.08 m and 1.07 m, corresponding to magnitudes between 6.3 and 7 (Tables 2 and 3). In Fig. 9b, where these values are represented against the scalar seismic moment, one can observe again no significant difference between intermediate-depth and deep events. For both types of earthquakes, an increase in maximum slip with size is observed, as shown (black line in Fig. 9b) by the relationship $\Delta u_{max} = 10^{-11\pm2} M_0^{0.53\pm0.08}$.

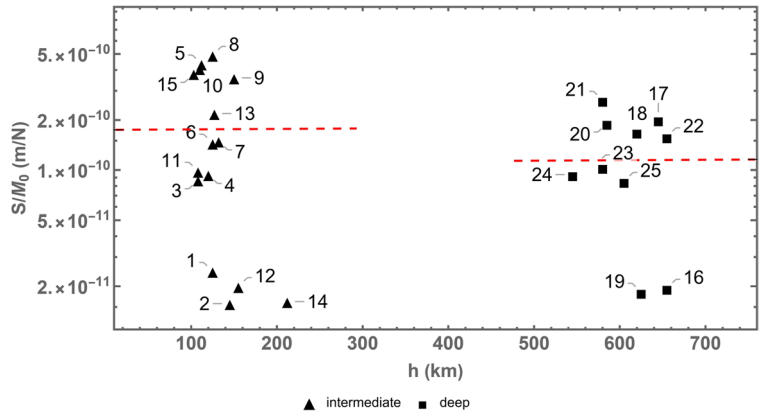

Fig. 10 Effective rupture area over scalar seismic moment versus depth. Dotted lines are the mean values for intermediate and deep earthquakes

Considering $\Delta u_{max}/M_0$, the values for intermediate-depth earthquakes are slightly larger than those for deep-depth earthquakes, as shown by the mean values (Fig. 11, dotted lines) for the two groups: $(6 \pm 1) \times 10^{-20}$ N^{-1} and $(2.5 \pm 0.7) \times 10^{-20}$ N^{-1} for intermediate- and deep-depth earthquakes, respectively. This result is similar to that found for rupture areas. For the intermediate-depth earthquakes, the events with greatest magnitude (event 1 and 2, $M_W = 7.5$ and 8.0 respectively) show the largest dispersion. The slip distributions over the rupture plane (Figs. 5 and 7 and Fig. S1-S25) show that for both types of earthquakes, the ruptures correspond in most cases to a single asperity, except for complex events 2 and 24 (in agreement with their complex STFs), as mentioned earlier.

The STFs of most intermediate- and deep-depth earthquakes in our study show a single and narrow pulse (Figs. 5 and 7 and Supplementary Material), with the seismic energy released very quickly (STF durations less than or equal to 25 s). In addition, we analyzed the relationship between STF duration and scalar seismic moment (Tables 2 and 3). We observed a linear relationship between the logarithm of STF duration and the logarithm of M_0 for intermediate-depth and deep earthquakes (black line in Fig. 9c), resulting in the following equation: STF duration $= 10^{-4.6 \pm 0.7} M_0^{0.29 \pm 0.04}$. Therefore, the time duration scales as the cube root of the moment, as has already been shown by several studies (Kanamori and Anderson 1975; Campus and Das 2000; Houston 2001; Persh and Houston 2004; Ye et al. 2016b).

The STF duration divided by M_0 is plotted versus depth (Fig. 12), showing a mean value for intermediate-depth earthquakes that is slightly higher than that for deep-depth earthquakes: $(1.9 \pm 0.4) \times 10^{-18}$ s/Nm and $(1.5 \pm 0.4) \times 10^{-18}$ s/Nm for intermediate and deep-depth earthquakes, respectively. In this case, there is a difference between the two types of earthquakes with slightly longer time durations for

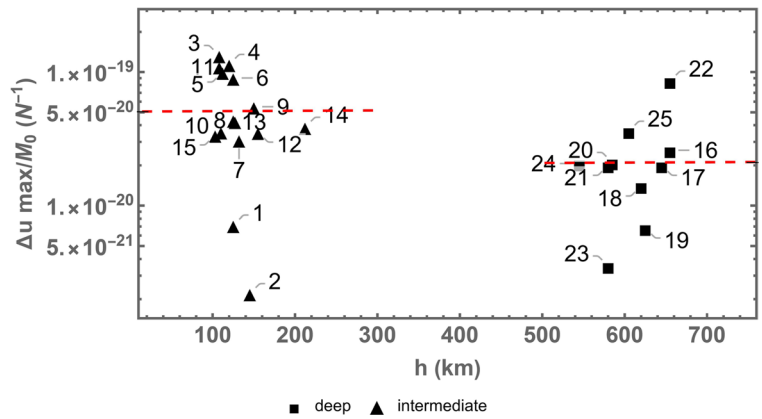

Fig. 11 Maximum slip over scalar seismic moment versus focal depth. Dotted lines are the mean values for intermediate-depth and deep earthquakes

intermediate-depth earthquakes. Four of them (events 1, 2, 12 and 14) with the largest magnitudes (7.5, 8.0, 7.1, and 7.1, respectively) have the lowest values; they are located in the northern part where the subducting slab is flat. The STFs of the intermediate-depth events (Fig. 5), located in the central and southern areas (12°S to 20°S), show that initially, only a small amount of energy is released, followed by, the main release (events 15, 10, 11, 13, 7 and 3). This situation is not observed for deep earthquakes. As mentioned earlier, special cases are earthquakes 2 and 25, with complex STFs. For deep-depth event 19, the STF presents two pulses and a duration of 17.5 s (Fig. 7), consistent with findings by Ye et al. (2016b), Zahradník et al. (2017), and Ruiz et al. (2017).

To carry out a comparison between the STFs of intermediate-depth and deep-depth earthquakes, we scaled the STF functions to a common size following the procedure of Houston et al. (1998). We normalized the STF of each earthquake for time and amplitude using the scalar seismic moment reference (M_{0ref}) of 10^{19} Nm, and then the average STF was estimated by multiplying the time axis by $\left({}^{M_{oref}}/_{M_0}\right)^{1/3}$ and the amplitude axis by $\left({}^{M_{oref}}/_{M_0}\right)^{2/3}$ for each earthquake (Kanamori and Anderson 1975). In Fig. 13, the scaled average STF for intermediate-depth (blue) and deep (red) events are shown. We see that although the duration is approximately the same for both types of events, the deep earthquakes (red curve) have a sharper increase in moments than the intermediate-depth earthquakes (blue curve). In the same Fig. 13, both average STF curves have two peaks. For deep events, the peaks are very close (at 4 s and 5 s) with similar amplitudes (1.8×10^{18} Nm and 1.7×10^{18} Nm), while for intermediate-depth earthquakes, the peaks are more separated (at 5 s and 9 s), and their amplitudes differ greatly; the first peak is larger than the second (1.8×10^{18} versus 1.0×10^{18} Nm). Event 24 (h = 545 km) was omitted from this calculation due to its STF complexity and larger moment at release (Fig. S24a).

Figure 13 shows that for the earthquakes in our study in the Peru-Bolivia-northern Chile region, both at intermediate-depth (100–300 km) and very deep (550–700 km) events have similar STFs displaying a certain complexity with two peaks. The peaks are very close in time and have similar amplitudes for the deep events, whereas there are somewhat larger differences in time and amplitudes for intermediate-depth events. These results are compatible with those obtained by Houston et al. (1998). In our study, we analyzed deeper earthquakes (between 562 and 636 km) using only one event (event 24 at 545 km) within the range of 350–550 km, where Houston et al. (1998) found greater complexity in the STF. This issue warrants further investigation in future studies.

The estimated E_R values (Tables 2 and 3) are in agreement with those obtained by IRIS (https://doi.org/10.17611/DP/EQE.1.) and other authors (Ye et al. 2016b; 2020; Ruiz et al. 2017), except for the intermediate-depth event 1, i.e., 1.9×10^{14} J in our study versus 2.6×10^{15} J obtained by IRIS (https://doi.org/10.17611/DP/19633278). In Fig. 9d, we observe a linear relationship between the logarithm of E_R and the logarithm of M_0 for intermediate-depth and deep earthquakes. The resulting fit (black line in Fig. 9d) is $E_R = 10^{-8\pm2}M_0^{1.2\pm0.1}$.

Figure 14 shows the E_R/M_0 (scaled energy) versus depth. The intermediate-depth earthquakes indicate large dispersion, with values from 0.1×10^{-6} to

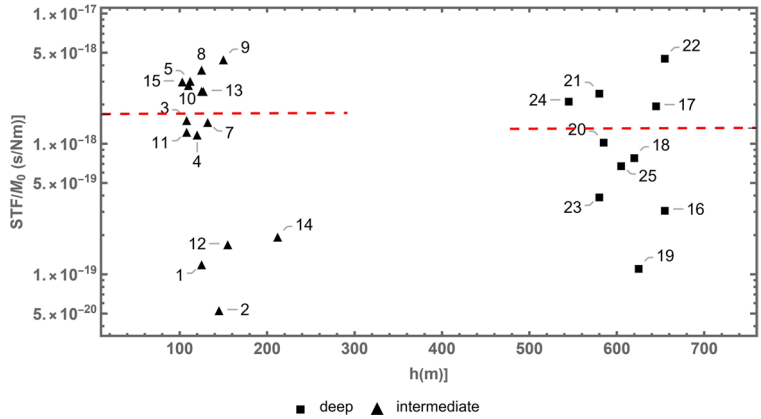

Fig. 12 Duration of the STF over the scalar seismic moment versus focal depth. Dotted lines are the mean values for intermediate-depth and deep earthquakes

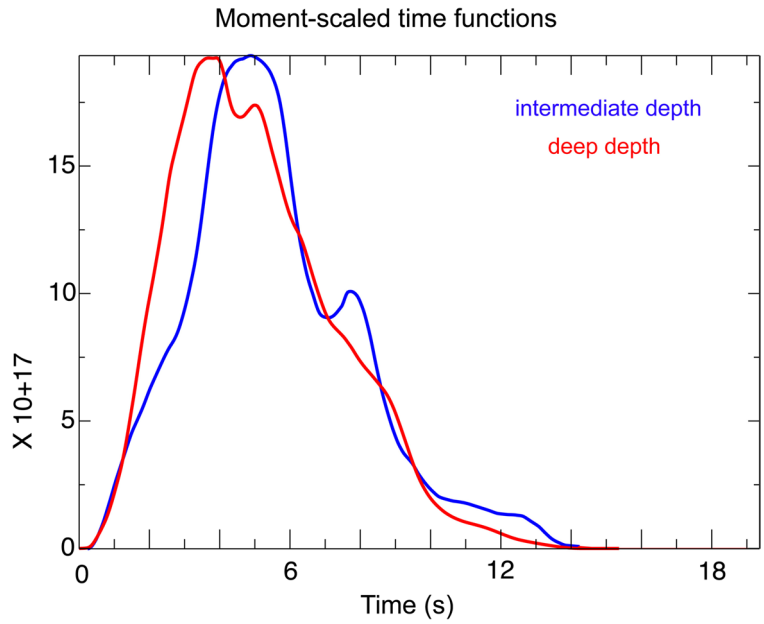

Fig. 13 Scaled average STF for intermediate-depth (blue) and deep events (red)

7×10^{-4}, while for the deep events, the ratio is higher, with values from 7×10^{-5} to 6×10^{-4}. The average value of the scaled energy is slightly larger for deep events ($(2.7\pm0.6)\times10^{-5}$) than for intermediate events ($(1.9\pm0.5)\times10^{-5}$). This result agrees with Poli and Prieto (2016) who found that deep earthquakes tend to be more efficient than the intermediate-depth earthquakes for the same subduction zone. However, as we cited previously, Tocheport et al. (2007) did not observe any variation in the scaled energy with depth.

Newman and Okal (1998) defined the energy-to-moment ratio factor θ as the logarithm of the scaled energy, which can identify source characteristics such as how slow or fast the rupture was. Convers and Newman (2011) obtained θ = -4.51 for events with a normal focal mechanism and θ = -4.74 for thrust events. In this work, from the average scaled energy, we obtained θ = -4.7 ± 0.3 for intermediate- and θ = -4.6 ± 0.2 for deep-depth events, which is not a significant difference. The apparent stress increases with depth, ranging from 0.1 to 4.4 MPa for intermediate earthquakes and from 0.7 to 7.6 MPa for deep events, with average values of 1.2 ± 0.3 MPa and 3.2 ± 0.7 MPa for intermediate and deep-depth earthquakes, respectively, which are in agreement with other authors (Poli and Prieto 2016).

Therefore, we observe differences in some rupture parameters between intermediate-depth and deep-depth earthquakes. The values of the effective rupture area, maximum slip and STF duration divided

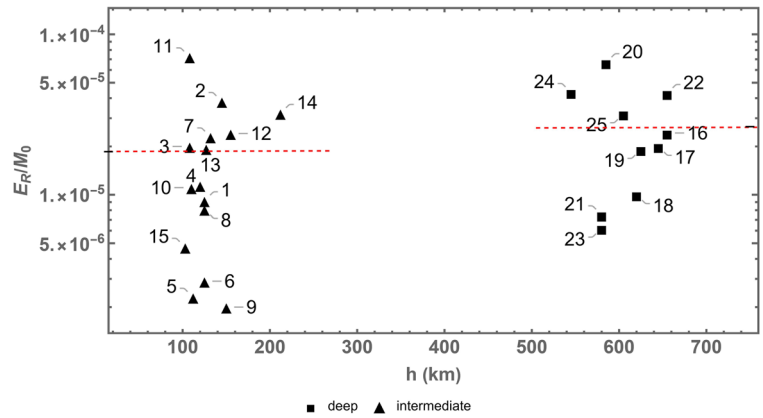

Fig. 14 Scaled radiated seismic energy versus depth. Dotted lines are the mean values for intermediate-depth and deep earthquakes

by the seismic moment for intermediate events are slightly larger than those for deep events, while the mean scaled energy is larger for deep earthquakes. This suggests a faster rupture process for deep events (Newman and Okal 1998; Convers and Newman 2011). Besides, the apparent stress also increases with depth in agreement with Liu et al. (2020), who obtained higher stress drop for deep-depth earthquakes than for shallow ones. They also observed wide variation, suggesting various mechanisms producing them. The differences found in our work may be related to a dependence of the rupture process on depth in the PBBNC region.

For deep depth earthquakes, a pure brittle rupture model seems to be unlikely due to the pressure and temperature conditions. Nevertheless, seismic observations indicate that the rupture process for shallow and deep earthquakes is similar despite different failure mechanisms and physical conditions (Billen 2020). Due to the complexity of deep earthquakes, there is no consensus on the best physical mechanism to explain their origin; even a dual-mechanism has been proposed (Zhan 2019). In this work, we obtained low values of stress drop for deep events that could be compatible with phase transformation mechanism (Zhan et al. 2014; Liu et al. 2020). Nevertheless, Zahradnik et al. (2017) by interpreting the seismic observations of the November 24, 2015, doublet that occurred in the Peru-Brazil region, concluded that a high-pressure variant of the dehydration embrittlement hypothesis was the most likely seismogenic mechanism. On the other hand, Billen (2020) asserted that the large gap in seismicity in the region (between 300 km -500 km) is inconsistent with any mechanism that is primarily controlled by temperature.

For intermediate- depth events the situation is similar and the dehydration embrittlement mechanism has been widely used to explain their origin (Hacker et al. 2003; Okazaki and Hirth 2016). In particular, for the Peru region, a relationship with the morphology of the slab has also been proposed (Lemoine et al. 2002; Liu and Yao 2020).

In our work, the stress drop values are similar for both intermediate and deep earthquakes, which agrees with Vallée (2013) and Poli and Prieto (2016). However, it is important to note that these estimations depend upon the assumed source model and may be subject to large uncertainties.

6 Source parameters and tectonic setting of the subduction zone

Tectonically, the intermediate-depth and deep-depth earthquakes, for which we have determined their source parameters, correspond to the northern part of the subduction of the Nazca plate beneath the South American plate. The tectonics of this region have been the object of numerous studies (for example: Dewey and Lamb 1992; Jaillard et al. 2000; Gutscher et al. 2000; Engdahl et al. 2020; Tavera et al. 2021). As already mentioned, there is a lack of earthquakes between depths of 300 and 500 km. At those depths, the subducting plate is either inactive or not present (Barcheck et al. 2012). According to Wortel (1984), the subducting Nazca plate is discontinuous, but for James and Snoke (1990), the plate is continuous, and the absence of earthquakes between depths of 300 and 500 km is due to a phase transition of the materials from brittle to ductile due to thermal variations within the subducting plate.

The parameters more directly related to the tectonic conditions are the focal mechanism orientations. Figure 15 shows the horizontal component of the T axes for both intermediate-depth and deep earthquakes. In the northern part (from 0° to 12°S), the stress pattern generally corresponds to an E−W horizontal extension, with the tensional axis perpendicular to the trench, indicating that the likely mechanism for deformation is slab pull according with previous studies of this subduction zone (Cahill and Isacks 1992; Slancova et al. 2000; Brudzinski and Chen 2005). South of 12°S, the T axes are not horizontal but dip between 30° and 53°. A small change in the horizontal orientation of the T axis may be observed from NE−SW in the northern part to E−W in the southern part. The observed differences in the T axis orientation agree with the geometry of the subduction zone. The horizontal extension observed for the intermediate-depth earthquakes in the northern part corresponds to the flat part of the subducting plate (Figs. 2a and 2b). In the southern part, the T axes of intermediate earthquakes dip approximately 30°, which is in agreement with the slope of the subducting slab. For this southern part, Bloch et al. (2018) correlated the increase in event rate of $M>7$ intermediate-depth earthquakes with the increase in the absolute slab pull component of the stress field.

In Fig. 16, we show the general geometry of the subduction zone in the region and the results of the

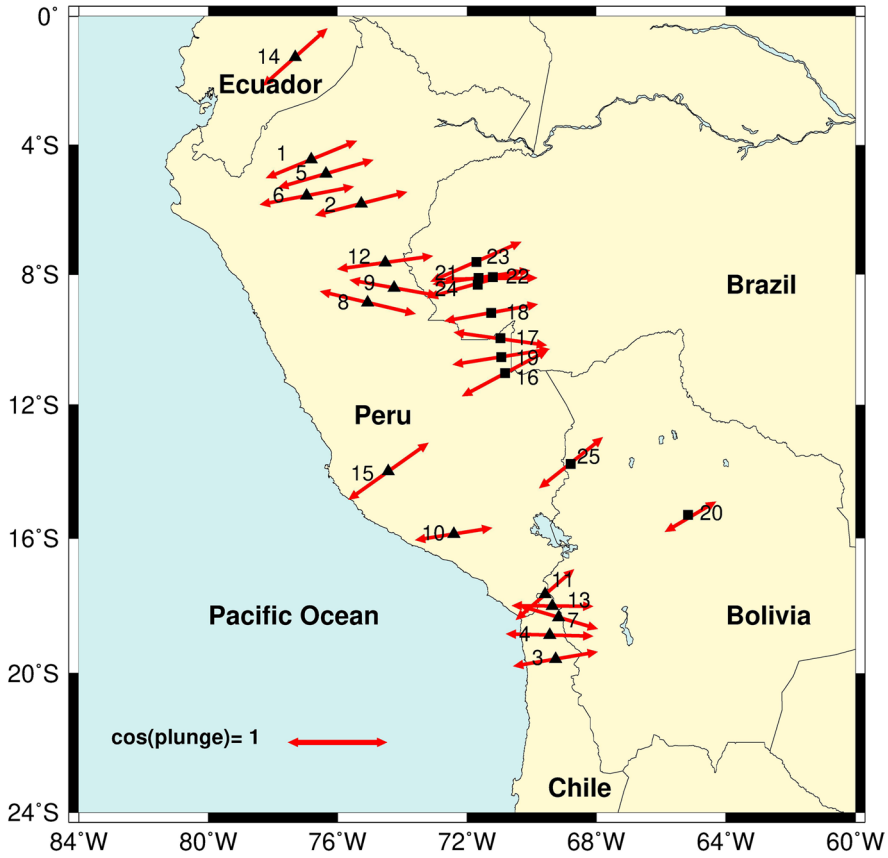

Fig. 15 Map showing the orientation of the horizontal projection of the tension axes

orientation of the stresses at intermediate and deep depths obtained in this study. To the north, to 12°S, the Nazca plate dips to the east under the American plate and changes into a flat slab at a depth of 100 km (Barazangi and Isacks 1976; Gutscher et al. 2000; Engdahl et al. 2020; Tavera et al. 2021). The studied intermediate-depth earthquakes, located at these latitude intervals, have occurred within this flat portion of the subducted slab and have focal mechanism solutions of normal motion with the T axis nearly horizontal and in an E−W orientation, which is typical for the events that occur at intermediate depths in the sub-Andean zone of Peru, showing the subducted plate being stretched outward (Tavera 2012). Between 13°S and 16°S, there is a transition zone in the subduction geometry, from flat to dipping 30°. Between the horizontal profile beneath central Peru and the 30° dipping plate in southern Peru, there is a contortion over a 100 km wide continuous lateral section of the subducting plate (Hasegawa and Sacks 1981). This change explains the focal mechanism of event 10, corresponding to dip-slip motion with the T axis dipping approximately 40° to the east. In northern Chile, between 17°S and 20°S, the subducted slab presents a slope of 30°, and in accordance, the corresponding intermediate events have a focal mechanism with T axes dipping 28°-35° to the east approximately parallel to the local dip of the descending Nazca plate. Therefore, intermediate-depth earthquakes within the descending slab have tension axes nearly parallel to the local dip of the slab, in agreement with Hasegawa and Sacks (1981). The complex rupture process for some intermediate-depth earthquakes may be explained in terms of a heterogeneous stress pattern due to the flexed geometry of the slab in the northern region where the slab changes from flat to sinking (Liu and Yao 2020).

The occurrence of deep earthquakes at latitudes of 6°–16°S and at a distance greater than 800 km from the trench may be explained by the vertical subduction of the lower part of the Nazca plate (Schneider and Sacks 1987; Bernal and Tavera 2001; Tavera and Buforn 2001). The focal mechanisms obtained in our study for the deep earthquakes located in the northern part have

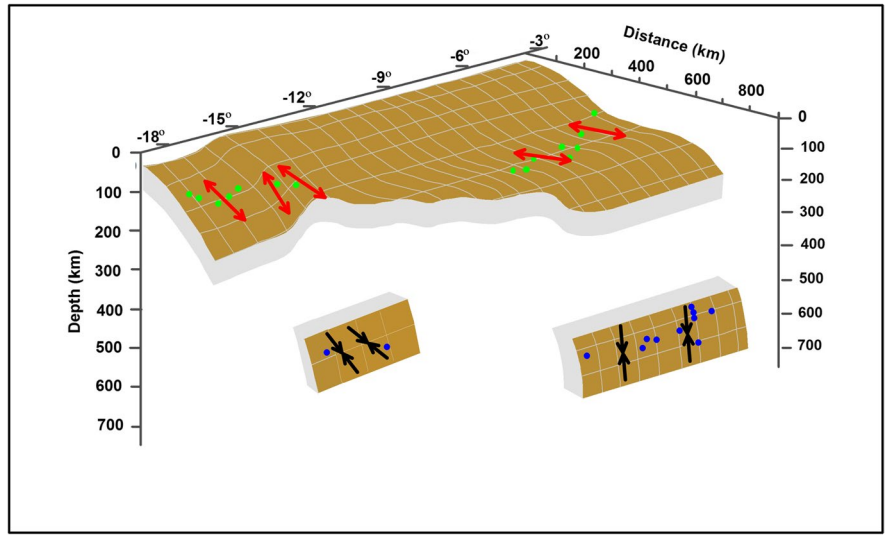

Fig. 16 Scheme of subduction in the region. Green circles correspond to the location of the studied intermediate-depth earthquakes, and blue circles correspond to deep earthquakes. Red arrows represent the T axes at intermediate depth, and black arrows represent the P axes at deep depth

a vertical pressure axis, showing vertical compression along the subducted plate. To the south, from 14°S to 16°S, the focal mechanisms for the deep events are different, showing dip-slip motion with the P axis dipping 45° to the NE (Fig. 15). These deep-focus earthquakes indicate a vertical segment of plate under axial compression at depths of 550–600 km (Stauder 1975). In conclusion, the obtained focal mechanisms agree with the general stress regime of the subducted slab corresponding to extension at intermediate depths and compression at the deepest depths.

7 Conclusions

From a study of the source parameters of 15 intermediate-depth and 10 deep earthquakes located in the PBBNC, we conclude the following:

- There are differences between the effective rupture areas and maximum slips for intermediate-depth and deep earthquakes, with higher values for intermediate-depth earthquakes. For intermediate-depth earthquakes, the lowest values correspond to events located along the flat subducting slab. Slip distributions, except for a few cases, correspond to simple ruptures. The STFs, in general, are single pulses, with larger time durations for intermediate depths and shorter durations for deep shocks and differences in the average shapes of the moment-scaled STFs. Values of the scaled energy show less dispersion and higher average values for deep earthquakes than for intermediate-depth earthquakes. The apparent stress also increases with depth.
- Based on the mechanism of earthquakes at intermediate depths, the stress regime pattern corresponds to horizontal extension in the north and extension dipping 30° in the south. At deep depths (500–700 km), the stress regime corresponds to vertical compression in the north and dips of approximately 45° in the south. These results are in agreement with the inferred geometry of the subduction of the Nazca plate, which has a flat part in the north, depths of approximately 100–120 km, and dips 30° from 500–700 km. In the south, the plate dips 30° continuously from the surface to 700 km.

8 Data and resources

Digital data have been obtained from Incorporated Research Institutions for Seismology (IRIS) (available at http://ds.iris.edu/wilber3/find_event; last accessed October 2023). Most data processing was done using SAC2000 software (available at http://ds.iris.edu/ds/nodes/dmc/software/downloads/sac; last accessed October 2023). Several of the plots in this paper were made using the Generic Mapping Tools software (Wessel and Smith 1998). The Kikuchi and Kanamori

codes for inversion and slip distribution are available at https://wwweic.eri.u-tokyo.ac.jp/ETAL/KIKUCHI/ (last accessed October 2023). Supplementary Material for this article includes the results obtained from the slip inversion for each event and for the two planes of the fault plane solution, together with the fit of the observed and synthetic seismograms.

Acknowledgements This work has been partially supported by the Spanish Ministry of Economy and Competitiveness (Project Number PID2021-122662OB-I00) and by the Proyecto de Investigación Santander-UCM (PR44/21-29929).

Author contributions The ruptures parameters were calculated by C.P., E.B. and L.E. The results were analyzed and interpreted by all authors. H.T. and E.C. contextualized with the tectonics of the study area and prepared figures 1, 2 and 16. C.P., E.B. and A.U. wrote the main manuscript text. M.M. analyzed the results and their relationship with the origin of intermediate and deep-depth earthquakes. All authors reviewed the manuscript and have approved the submitted version.

Funding Open Access funding provided thanks to the CRUE-CSIC agreement with Springer Nature.

Declarations

Competing interests The authors declare no competing interests.

References

Barazangi M, Isacks B (1976) Spatial distribution of earthquakes and subduction of the Nazca Plate beneath South America. Geology J. 686–692, 1976. https://doi.org/10.1130/0091-7613(1976)4<686:SDOEAS>2.0.CO;2

Barcheck CG, Wiens DA, van Keken PE, Hacker BR (2012) The relationship of intermediate- and deep-focus seismicity to the hydration and dehydration of subducting slabs. Earth Planet Sci Lett 349–35:153–160. https://doi.org/10.1016/j.epsl.2012.06.055

BDSN (2014) Berkeley Digital Seismic Network. UC Berkeley Seismological Laboratory. Dataset. https://doi.org/10.7932/BDSN

Bernal I, Tavera H (2001) Geodynamics, Seismicity and Seismic Energy in Peru, Monographs Series, Geophysical Institute of Peru, Lima, Peru, 64 pp. (in Spanish)

Billen MI (2020) Deep slab seismicity limited by rate of deformation in the transition zone. Sci Adv. 6 (22), eaaz7692

Bloch W, Schurr B, Kummerow J, Salazar P, Shapiro SA (2018) From slab coupling to slab pull: Stress segmentation in the subducting Nazca plate. Geophys Res Lett 45:5407–5416. https://doi.org/10.1029/2018GL078793

Boatwright J, y Choy GL (1986) Teleseismic estimates of the energy radiated by shallow earthquakes. J Geophys Res Solid Earth. 91(B2), 2095-2112 https://doi.org/10.1029/JB091iB02p02095

Brudzinski MR, Chen WP (2005) Earthquakes and strain in subhorizontal slabs. J Geophys Res 110. https://doi.org/10.1029/2004JB003470

Cabrera L, Ruiz S, Poli P, Contreras-Reyes E, Osses A, Mancini R (2021) Northern Chile intermediate-depth earthquakes controlled by plate hydration. Geophys J Int 226(1):78–90. https://doi.org/10.1093/gji/ggaa565

Cahill T, Isacks B (1992) Seismicity and shape of the subducted Nazca Plate. J Geophys Res 97:17503–17529. https://doi.org/10.1029/92JB00493

Campus P, Das S (2000) Comparison of the rupture and radiation characteristics of intermediate and deep earthquakes. J Geophys Res 105:6177–6189. https://doi.org/10.1029/1999JB900384

Carebbean Network (2006). Albuquerque Seismological Laboratory (ASL)/USGS. International Federation of Digital Seismograph Networkshttps://doi.org/10.7914/SN/CU

Convers JA, Newman AV (2011) Global Evaluation of Large Earthquake Energy from 1997 Through mid-2010. J Geophys Res. 116

Derode B, Campos J (2019) Energy budget of intermediate-depth earthquakes in northern Chile: Comparison with shallow earthquakes and implications of rupture velocity models used. Geophys Res Lett 46:2484–2493. https://doi.org/10.1029/2018GL080962

Dewey JF, Lamb SH (1992) Active Tectonics of the Andes. Tectonophysics 205:79–95

Engdahl ER, Di Giacomo D, Sakarya B, Gkarlaouni CG, Harris J, Storchak DA (2020) ISC-EHB 1964–2016, an improved data set for studies of Earth structure and global seismicity. Earth Space Sci. 7:e2019EA000897. https://doi.org/10.1029/2019EA000897

GEOFON (1993). GEOFON Seismic Network. GFZ Data Services. Other/Seismic Network. https://doi.org/10.14470/TR560404

GEOSCOPE (1982) Institut de physique du globe de Paris (IPGP) and Ecole et Observatoire des Sciences de la Terre de Strasbourg (EOST). French global network of broad band seismic stations. Institut de physique du globe de Paris (IPGP), Université de Paris. https://doi.org/10.18715/GEOSCOPE.G

GSN IRIS/IDA (1986) Scripps Institution of Oceanography. Global Seismograph Network - IRIS/IDA . International Federation of Digital Seismograph Networks. https://doi.org/10.7914/SN/II

GSN IRIS/USGS (2014) Albuquerque Seismological Laboratory/USGS. Global Seismograph Network (GSN - IRIS/

USGS) . International Federation of Digital Seismograph Networks. https://doi.org/10.7914/SN/IU
GTSN (1993) Albuquerque Seismological Laboratory (ASL)/ USGS. Global Telemetered Seismograph Network (USAF/USGS) . International Federation of Digital Seismograph Networks. https://doi.org/10.7914/SN/GT
Green HW (2007) Shearing instabilities accompanying high-pressure phase transformations and the mechanics of deep earthquakes. Proc Natl Acad Sci USA 104:9133–9138
Gutscher M, Spakman W, Bijwaard H, Engdahl E (2000) Geodynamics of flat subduction: Seismicity and tomographic constraints from the Andean margin. Tectonics 19(5):814–833. https://doi.org/10.1029/1999TC001152
Hacker BR, Peacock SM, Abers GA, Holloway SD (2003) Subduction factory 2: are intermediate-depth earthquakes in subducting slabs linked to metamorphic dehydration reactions? J Geophys Res Solid Earth. 108 (B1), 2030
Hayes GP, Wald DJ, Johnson RL (2012). Slab1.0: A three-dimensional model of global subduction zone geometries. J Geophys Res. 117: B01302. https://doi.org/10.1029/2011JB008524.
Hasegawa A, Sacks IS (1981) Subduction of the Nazca Plate Beneath Peru as determined from seismic observations. J Geophys Res 86(B6):4971–4980. https://doi.org/10.1029/JB086iB06p04971
Houston H (2001) Influence of depth, focal mechanism, and tectonic setting on the shape and duration of earthquake source time functions. J Geophys Res 106(B6):11137–11150. https://doi.org/10.1029/2000JB900468
Houston H, Benz HM, Vidale JE (1998) Time functions of deep earthquakes from broadband and short-period stacks. J Geophys Res. 103, 29,895 – 29,913. https://doi.org/10.1029/98JB02135
Hu Y, Yagi Y, Okuwaki R, Shimizu K (2021) Back-propagating rupture evolution within a curved slab during the 2019 M_W 8.0 Peru intraslab earthquake. Geophys J Int 227:1602–1611
IMS (1965) Various Institutions. International Miscellaneous Stations . International Federation of Digital Seismograph Networks. https://doi.org/10.7914/vefq-vh75
Jaillard E, Herail G, Monfret T, Díaz-Martínez E, Baby P, Lavenu A, Dumont JF (2000) Tectonic evolution of the Andes of Ecuador, Peru, Bolivia and Northernmost Chile. In U. G. Cordani, E. J. Milani, A. Thomaz Filho, and D. A. Campos, Tectonic Evolution of South America, (31 International Geological Congress, Rio de Janeiro), 481–559
James D, Snoke J (1990) Seismic evidence for continuity of the deep slab beneath central and eastern Peru. J Geophys Res 95:4989–5001. https://doi.org/10.1029/jb095ib04p04989
Jiménez C, Luna N, Moreno N, Saavedra M (2021) Seismic source characteristics of the intermediate-depth and intraslab 2019 northern Peru earthquake (M_W 8.0). J Seismol 25:863–874. https://doi.org/10.1007/s10950-021-09996-x
John T, Medvedev S, Rupke LH, Andersen TB, Podladchikov YY, Aussrheim H (2009) Generation of intermediate-depth earthquakes by self-localizing thermal runaway. Nat Geosci 2:137–140
Kanamori H, Anderson DL (1975) Theoretical basis of some empirical relations in seismology. Bull Seismol Soc Am 65:1073–1095
Kanamori H, Anderson DL, Heaton TH (1998) Frictional melting during the rupture of the 1994 Bolivian earthquake. Science 279:839–842
Karato S, Riedel MR, Yuen DA (2001) Rheological structure and deformation of subducted slabs in the mantle transition zone: Implications for mantle circulation and deep earthquakes. Phys Earth Planet Inter 127:83–108
Kennett BLN, Engdahl ER (1991) Travel-times for global earthquake location and phase identification. Geophys J Int 105:429–465. https://doi.org/10.1111/j.1365-246X.1991.tb06724.x
Kikuchi A, Kanamori H (1991) Inversion of complex waves III. Bull Seismol Soc Am 81:2335–2350
Ko JY-T, Kuo B-Y (2016) Low radiation efficiency of the intermediate-depth earthquakes in the Japan subduction zone. Geophys Res Lett 43:11611–11619. https://doi.org/10.1002/2016GL070993
Lemoine A, Madariaga R, Campos J (2002) Slab-pull and slab-push earthquakes in the Mexican, Chilean and Peruvian subduction zones. Phys Earth Planet Inter 132(1–3):157–175. https://doi.org/10.1016/S0031-9201(02)00050-X
Lay T, Ye L, Kanamori H, Yamazaki Y, Cheung KF, Koper KD, Kwong K (2013) The October 28, 2012 M_W 7.8 Haida Gwaii underthrusting earthquake and tsunami: Slip partitioning along the Queen Charlotte Fault transpressional plate boundary. Earth Planet Sci Lett 375:57–70. https://doi.org/10.1016/j.epsl.2013.05.005
Lim H, Kima Y, Clayton RW, Thurber CH (2018) Seismicity and structure of Nazca Plate subduction zone in southern Peru. Earth Planet Sci Lett 498: 334–347
Lindo R, Dorbath C, Cisternas A, Dorbath L, Ocola L, Morales M (1992) Subduction geometry in central Peru from a microseismicity survey: first results. Tectonophysics 205:23–29. https://doi.org/10.1016/0040-1951(92)90415-3
Liu W, Yao H (2020) Rupture process of the 26 May 2019 MW 8.0 northern Peru intermediate-depth earthquake and insights into its mechanism. Geophys Res Lett 47:e2020GL087167. https://doi.org/10.1029/2020GL087167
Liu M, Huang Y, Ritsema J (2020) Stress drop variation of deep-focus earthquakes based on empirical Green's functions. Geophys Res Lett 47:e2019GL086055. https://doi.org/10.1029/2019GL086055
Megawati M, Ma K-F, Chen P-F, Sianipar D, Hsieh M-C, (2024) Source characterization of intermediate-depth earthquakes in Southern Java, Indonesia. J Asian Earth Sci. https://doi.org/10.1016/j.jseaes.2024.106040
Newman AV, Okal EA (1998) Teleseismic estimates of radiated seismic energy: The E/M0 discriminant for tsunami earthquakes. J Geophys Res 103:26885–26898
Nishitsuji Y, Mori J (2014) Source parameters and radiation efficiency for intermediate-depth earthquakes in Northeast Japan. Geophys J Int 196:1247–1259. https://doi.org/10.1093/gji/ggt458
Norabuena E, Snoke A, James D (1994) Structure of the subducting Nazca plate beneath Peru. J Geophys Res 99:9215–9226. https://doi.org/10.1029/94JB00126
Norabuena E, Leffier-Griffin L, Mao A, Dixon T, Stein S, Sacks IS, Ocola L, Ellis M (1998) Space geodetic observations of Nazca-South America convergence across the

Central Andes. Science 279:358–362. https://doi.org/10.1126/science.279.5349.358

Omori S, Komabayashi T, Maruyama S (2004) Dehydration and earthquakes in the subducting slab: Empirical link in intermediate and deep seismic zones. Phys Earth Planet Inter 146:297–311

Okazaki K, Hirth G (2016) Dehydration of lawsonite could directly trigger earthquakes in subducting oceanic crust. Nature 530:81–84

Park S-C, Mori J (2008) Rupture velocity estimation of large deep-focus earthquakes surrounding Japan. J Geophys Res 113:B08303. https://doi.org/10.1029/2007JB005434

Persh SE, Houston H (2004) Deep earthquake rupture histories determined by global stacking of broadband P waveforms. J Geophys Res 109:B04311. https://doi.org/10.1029/2003JB002762

Phillips K, Clayton RW, Davis P, Tavera H, Guy R, Skinner S, Stubailo I, Audin L, Aguilar V (2012) Structure of the subduction system in southern Peru from seismic array data. J Geophys Res 117:B11306. https://doi.org/10.1029/2012JB009540

Poli P, Prieto GA (2016) Global rupture parameters for deep and intermediate-depth earthquakes. J Geophys Res 121(12):8871–8887

Prieto GA, Florez M, Barrett SA, Beroza GC, Pedraza P, Blanco JF, Poveda E (2013) Seismic evidence for thermal runaway during intermediate-depth earthquake rupture. Geophys Res Lett 40(23):6064–6068

Roberts DC, Turcotte DL (2000) Earthquakes: Friction or plastic instability? Geocomplexity Phys Earthquakes 120:97–103. https://doi.org/10.1029/GM120p0097

Rodkin MV (2022) The Variability of Earthquake Parameters with the Depth: Evidences of Difference of Mechanisms of Generation of the Shallow, Intermediate-Depth, and the Deep Earthquakes. Pure Appl Geophys 179:4197–4206. https://doi.org/10.1007/s00024-021-02927-4

Ruiz S, Tavera H, Poli P, Herrera C, Flores C, Rivera E, Madariaga R (2017) The deep Peru 2015 doublet earthquakes. Earth Planet Sci Lett 478:102–109. https://doi.org/10.1016/j.epsl.2017.08.036

Schneider J, Sacks S (1987) Stress in the Contorted Nazca Plate beneath southern Peru form local earthquakes. J Geophys Res 92:13887–13902. https://doi.org/10.1029/JB092iB13p13887

SCSN (1926) California Institute of Technology and United States Geological Survey Pasadena. Southern California Seismic Network . International Federation of Digital Seismograph Networks. https://doi.org/10.7914/SN/CI

Slancova A, Spicak A, Hanus V, Vanek J (2000) Delimination of domains with uniform stress in the subducted Nazca plate. Tectonophysics 319:339–364. https://doi.org/10.1016/S0040-1951(99)00302-9

Spence W, Mendoza C, Engdahl ER, Choy GL, Norabuena E (1999) Seismic subduction of the Nazca ridge as shown by the 1996–97 Peru earthquakes. Pure Appl Geophys 154:753–776. https://doi.org/10.1007/s000240050251

Stauder W (1975) Subduction of the Nazca plate under Peru as evidenced by focal mechanisms and by seismicity. J Geophys Res 80(1053–1064):1975. https://doi.org/10.1029/JB080i008p01053

Suzuki M, Yagi Y (2011) Depth dependence of rupture velocity in deep earthquakes. Geophys Res Lett 38:L05308. https://doi.org/10.1029/2011GL046807

Tamay J, Galindo-Zaldivar J, Soto J, Gil AJ (2021) GNSS Constraints to Active Tectonic Deformations of the South American Continental Margin in Ecuador. Sensors 21:4003. https://doi.org/10.3390/s21124003

Tavera H (2012) A report on the 24 August 2011 M w 7.0 Contamana, Peru, intermediate-depth earthquake. Seismol Res Lett. 83(6): 1007–1013. https://doi.org/10.1785/0220120005

Tavera H (2023) Sismicidad en Perú. Boletín del Instituto Geofísico del Perú. 35 pp. (in Spanish)

Tavera H, Buforn E (2001) Source mechanisms of earthquakes in Peru. J Seismol 5:519–539. https://doi.org/10.1023/A:1012027430555

Tavera H, Delouis B, Mercado A, Portugal D (2021) Loreto Intermediate Depth Earthquake of 26 May 2019 (Northeast Peru): Source Parameters by Inversion of Local to Regional Waveforms and Strong-Motion Observations. Seismol Res Lett 92(6):3349–3359. https://doi.org/10.1785/0220200459

Tibi R, Bock G, Wiens DA (2003) Source characteristics of large deep earthquakes: Constraint on the faulting mechanism at great depths. J Geophys Res 108(B2):2091. https://doi.org/10.1029/2002JB001948

Tocheport A, Rivera L, Chevrot S (2007) A systematic study of source time functions and moment tensors of intermediate and deep earthquakes. J Geophys Res 112:B07311. https://doi.org/10.1029/2006JB004534

Vallée M (2013) Source time function properties indicate a strain drop independent of earthquake depth and magnitude. Nat Commun. 4 https://doi.org/10.1038/ncomms3606.

Venkataraman A, y Kanamori H (2004) Observational constraints on the fracture energy of subduction zone earthquakes. J Geophys Res Solid Earth. 109(B5). https://doi.org/10.1029/2003JB002549

Villegas-Lanza JC, Chlieh M, Cavalie O, Tavera H, Baby P, Chire-Chira J, Nocquet JM (2016) Active tectonic of Peru: Heterogeneous inter-seismic coupling along the Nazca megathrust, rigid motion of the Peruvian Sliver, and Sub-Andean shortening accommodation. J Geophys Res 121:7371–7394. https://doi.org/10.1002/2016JB013080

Wagner LS, Okal EA (2019) The Pucallpa Nest and its constraints on the geometry of the Peruvian Flat Slab. Tectonophysics 762:97–108. https://doi.org/10.1016/j.tecto.2019.04.021

Wessel P, Smith WH (1998) New improved version of the Generic Mapping Tools release. Eos Trans AGU 79:579

Wortel M (1984) Spatial and temporal variations in the Andean subduction zone. J Geol Soc London 141:783–791. https://doi.org/10.1144/gsjgs.141.5.0783

Ye L, Lay T, Kanamori H (2013) Ground shaking and seismic source spectra for large earthquakes around the megathrust fault offshore of northeastern Honshu, Japan. Bull Seismol Soc Am 103(2B):1221–1241. https://doi.org/10.1785/0120120115

Ye L, Lay T, Kanamori H, Rivera L (2016a) Rupture characteristics of major and great ($M_W \geq 7.0$) megathrust earthquakes from 1990–2015: 1. Source parameter scaling relationships. J Geophys Res Solid Earth 121:826–844

Ye L, Lay T, Kanamori H, Zhan Z, Duputel Z (2016b) Diverse rupture processes in the 2015 Peru deep earthquake doublet. Sci Adv 2:6. https://doi.org/10.1126/sciadv.1600581

Ye L, Lay T, Kanamori H (2020) Anomalously low aftershock productivity of the 2019 M_W 8.0 energetic intermediate-depth faulting beneath Peru. Earth Planet Sci Lett. 549, 116528. https://doi.org/10.1016/j.epsl.2020.116528

Zahradník J, Čížková H, Bina CR, Sokos E, Janský J, Tavera H, Carvalho J (2017) A recent deep earthquake doublet in light of long-term evolution of Nazca subduction. Scientific Reports 7:45153. https://doi.org/10.1038/srep45153

Zhan Z (2020) Mechanisms and Implications of Deep Earthquakes. Annu Rev Earth Planet Sci 48:147–174. https://doi.org/10.1146/annurev-earth-053018-060314

Zhan Z, Kanamori H, Tsai VC, Helmberger DV, Wei S (2014) Rupture complexity of the 1994 Bolivia and 2013 Sea of Okhotsk deep earthquakes. Earth Planet Sci 385:89–96